Atmospheric Research 244 (2020) 105051

Contents lists available at ScienceDirect

Atmospheric Research

journal homepage: www.elsevier.com/locate/atmosres

Sea-land breeze diurnal component and its interaction with a cold front on the coast of Sisal, Yucatan: A case study

Ma. Eugenia Allende-Arandía[a,b,c,*], Jorge Zavala-Hidalgo[d], Alec Torres-Freyermuth[a,b], Christian M. Appendini[a,b], Ruth Cerezo-Mota[a,b,c], Nidia Taylor-Espinosa[d]

[a] Laboratorio de Ingeniería y Procesos Costeros, Instituto de Ingeniería, Universidad Nacional Autónoma de México, Sisal, Yucatán, 97356, Mexico
[b] Laboratorio Nacional de Resiliencia Costera (LANRESC), Laboratorios Nacionales CONACYT, Mexico
[c] Cátedras-CONACyT, Consejo Nacional de Ciencia y Tecnología, Ciudad de México, Mexico
[d] Centro de Ciencias de la Atmósfera, Universidad Nacional Autónoma de México, Coyoacán, Ciudad de México, 04510, Mexico

ARTICLE INFO

Keywords:
Sea breeze
Land breeze
Cold Surge
Diurnal signal
Yucatan Peninsula
WRF model

ABSTRACT

The breeze phenomenon is of great importance in coasts around the world owing to both its impact on local atmospheric dynamics and its influence on coastal processes. The northwest of the Yucatan Peninsula (YP) is characterized by the presence of intense sea breezes and Cold Surge (CS) events (locally known as Nortes). Field observations suggest that nearshore hydrodynamics and beach evolution in the study area are strongly controlled by waves generated during sea breeze events. In this paper, the diurnal wind component associated with the breeze phenomenon and its variability due to the presence of a CS event are investigated utilizing the Weather Research and Forecasting (WRF) model. The WRF model is implemented in three nested domains with a maximum resolution of 3.6-km. The numerical model was validated with observations at 20 stations located across the YP, adequately reproducing wind speed and direction at Sisal, Yuc. coast, with a correlation coefficient of 0.56 and a circular correlation coefficient of 0.83, respectively. Diurnal wind components were least-squares fitted to a sinusoidal signal, and the resulting parameters were used to obtain an elliptical hodograph related to the breeze phenomenon. Numerical results suggest that sea breezes, with wind intensities higher than 10 ms^{-1}, extend more than 100 km offshore in the northern YP. Although breeze events are caused by differential heating at a small spatial scale, particularly in the Gulf of Mexico, this diurnal signal exceeds the local spatial scale. Furthermore, the interaction between the sea breeze and the mean wind associated to the trade winds generates a line of convergence that crosses the YP. Model results allow us to identify that the mechanisms responsible of such large amplitude of the diurnal signal in this area are: (i) the thermal gradient, (ii) the relatively small value of the Coriolis force, (iii) the orography, (iv) the friction, and (v) the peninsula's geometry. The numerical results revealed that during the interaction between local breezes and a CS event, the diurnal signal remains, except for the initial day of the event. However, further research is needed to generalize the current results for other CS events with different intensity and displacement characteristics.

1. Introduction

Breezes are a local mesoscale wind system that characterizes the coastal regions around the world (Gille et al., 2005). Their main driving mechanism is the temperature gradient between the land and the ocean, leading to a change in atmospheric pressure and humidity of the air parcels, forming a circulation cell perpendicular to the coast with diurnal variation (Hughes and Veron, 2018). The importance of breezes is that they help to release heat near the surface, triggering the formation of electrical storms, increasing the humidity of the environment, and generating local wind waves. Furthermore, they can improve or worsen the quality of the air in the coastal zone (Gentry and Moore, 1954; Kozo, 1982; Yan and Anthes, 1988; Novitsky et al., 1992; Asimakopoulos et al., 1999; Van Delden, 2000; Day et al., 2010; Hsu, 2013; Hu and Xue, 2015; Kishtawal et al., 2016), as well as stir the coastal circulation responsible for near-shore sediment and pollutant transport (Masselink and Pattiaratchi, 1998a, 1998b; Hendrickson and MacMahan, 2009; Giffen et al., 2012; Torres-Freyermuth et al., 2017;

* Corresponding author at: Laboratorio de Ingeniería y Procesos Costeros, Instituto de Ingeniería, Universidad Nacional Autónoma de México, Sisal, Yucatán, 97356, Mexico.
E-mail addresses: mallendea@iingen.unam.mx (M.E. Allende-Arandía), jzavala@atmosfera.unam.mx (J. Zavala-Hidalgo), atorresf@iingen.unam.mx (A. Torres-Freyermuth), cappendinia@iingen.unam.mx (C.M. Appendini), rcerezom@iingen.unam.mx (R. Cerezo-Mota).

https://doi.org/10.1016/j.atmosres.2020.105051
Received 28 February 2019; Received in revised form 17 April 2020; Accepted 15 May 2020
Available online 17 May 2020

Medellín et al., 2018).

The characteristics of breezes, including their formation, duration, penetration, termination, and intensity, have been studied using both observations and numerical models (Gentry and Moore, 1954; Estoque, 1962; Novitsky et al., 1992; Atkins and Wakimoto, 1997; Asimakopoulos et al., 1999; Gille et al., 2003; Srinivas et al., 2006; Taylor-Espinosa, 2009; Papanastasiou et al., 2010; Azorin-Molina et al., 2011). Prior studies have already described breeze dynamics in detail (Arritt, 1993; Wakimoto and Atkins, 1994; Kingsmill, 1995; Atkins et al., 1995; Simpson, 1996; Atkins and Wakimoto, 1997; Stephan et al., 1999). However, depending on their geographical location, breezes are limited or modulated by the topography, low-level local winds, atmospheric stability (Leopold, 1949; Manobianco et al., 2005; Hughes and Veron, 2018), and their interaction with synoptic-scale atmospheric events. The relationship and interaction between the synoptic and local-scale atmospheric events modulate their propagation inland or offshore (Hughes and Veron, 2018). Gentry and Moore (1954) show that the interaction of offshore winds with the sea breeze circulation generates an area of convergence at low levels, which can develop more convection than the heating of the surface itself. Therefore, it is important to conduct site-specific studies that allow a better understanding of their variability.

The Yucatan Peninsula is characterized by both breeze and Cold Surge (CS) events. The latter are associated with the cold-front passage over the Gulf of Mexico and they occur during autumn, winter, and spring months (Manobianco et al., 2005; Figueroa-Espinoza et al., 2014). The CS events are cold and dry air masses from high latitudes and are associated with an increase in wind speed, a decrease in temperature, and an increase in atmospheric pressure over eastern Mexico, the Gulf of Mexico, and Central America (López-Méndez, 2009). The frequency of CSs at mid-latitudes varies with certain seasonality on a synoptic scale, occurring mainly when winds from the east weaken (Miller et al., 2003). The arrival frequency of a cold front and its latitudinal extent are a function of the position, magnitude, and amplitude of the mid-latitude circulation (DiMego et al., 1976). A thorough description of previous studies on CSs is found in Appendini et al. (2018).

This study aims to investigate the diurnal breeze variability in the northwest of the Yucatan Peninsula and the influence a CS event can have on it. The Weather Research and Forecasting (WRF) model is used to conduct a numerical study in that region. Firstly, the study area is described in Section 2. The data sets, numerical model setup and its validation are described in Section 3. The WRF model simulation of the meteorological conditions that occurred during a field experiment conducted in 2014 (Torres-Freyermuth et al., 2017) is employed to investigate the diurnal breeze component, the mean conditions, and the effect of a CS event on the breezes dynamics, and this is described in Section 4. Finally, concluding remarks are presented in Section 5.

2. Study area

The Yucatan Peninsula (YP) is located in the southeast of the Gulf of Mexico (GoM). This study is focused in Sisal, Yucatan, Mexico, located in the northwestern YP (21° 09′ 56.20” N, 90° 02′ 26.44” W) (Fig. 1). This coastal area is characterized by an *E*-W shoreline orientation, low-lying topography, and dominant winds associated with breeze events (Figueroa-Espinoza et al., 2014). These events determine the dynamics of the ocean circulation from the inner shelf to the surf zone (Enriquez et al., 2010; Ponce de León and Orfila, 2013; Torres-Freyermuth et al., 2017) and they are more frequent and intense during the months of spring and summer (April–August). The study area presents high mesoscale atmospheric variability with a well-defined seasonality. The summer months are characterized by the formation of low-pressure systems which give rise to intense cyclonic activity (Zavala-Hidalgo et al., 2014; Appendini et al., 2014), also associated with the Easterly Waves (Molinari et al., 1997; Serra et al., 2010). During the rest of the year, the region is affected by polar air masses that arrive as cold fronts (Manobianco et al., 2005; Figueroa-Espinoza et al., 2014), inducing a significant decrease in temperature and isolated rain events.

3. Data and methods

The period of study corresponds to the **N**earshore **C**oastal dynamics on a **S**ea-breeze dominated micro-tid**AL** beach (NCSAL) field experiment (Torres-Freyermuth et al., 2017) conducted from April 1st to April 12, 2014. During this period, nine breeze events were identified (seven events from April 1st to April 7 and two events from April 11 to April 12) and a CS event reached the study area on April 8 that lasted three days. To investigate the atmospheric dynamics, we used the Weather Research and Forecasting (WRF) numerical model. The model was validated on a regional scale using measured data from Automatic Weather Stations (AWS) and meteorological stations. After validation, the model was used to investigate the breeze dynamics in Sisal.

3.1. Datasets

For comparison of the model outputs with observations, we used data from 24 meteorological stations in the YP region. However, we only considered the 20 stations containing more than 95% of wind speed valid data (neither extreme [± 2 standard deviation] or zero values [more than a couple of continuous hours]) for the study period. The selected stations consisted of 17 AWS distributed across the states of Campeche, Yucatan, and Quintana Roo (data provided by the National Meteorological Service of Mexico), two stations located in Campeche and Yucatan belonging to the Mexican Navy (SEMAR for its acronym in Spanish), and one ultrasonic anemometer (UA) deployed in the Yucatan coast (LIPC UNAM, 2017) (Figueroa et al., 2014) (see Fig. 1b). The variables analyzed from each meteorological station were: 10 m zonal u and meridional v wind components (ms^{-1}) and wind direction (^{o}), and temperature (°C) at 2 m. All data were checked for quality control and, subsequently, low-pass filtered with a 1-h cut-off frequency. The raw data of the AWS had a sampling interval of 10 min, while the SEMAR data had a 15 min interval; therefore, the data measured every 60 min was used. Furthermore, coastal winds were measured at high-frequency (6 Hz) with the UA installed in a 50-m tower located 120 m inland and 6 m above the ground in Sisal, Yucatan.

3.2. Numerical model

In the present study, the Weather Research and Forecasting model (WRF) (WRFV.3.6.1.) (Skamarock et al., 2008) developed by the National Center for Atmospheric Research (NCAR) was implemented. This numerical model has been widely employed for research (Challa et al., 2009; Papanastasiou et al., 2010; Giffen et al., 2012; Ponce de León and Orfila, 2013; Fita et al., 2013; Carvalho et al., 2012, 2014; Hu and Xue, 2015; Kishtawal et al., 2016) and weather prediction (Givati et al., 2012; Schwartz, 2014). The WRF model is characterized by being compressible, non-hydrostatic, with terrain-following hydrostatic pressure vertical coordinates and an Arakawa-C horizontal grid staggered. The model uses the Runge-Kutta 2nd and 3rd order time integration schemes and the 2nd to 6th order advection schemes in both the horizontal and vertical. It also uses a small time-split step for acoustic and gravity-wave modes. For further details, interested readers are referred to Skamarock et al. (2008).

3.2.1. Model setup

The model physics parameterization schemes adopted in this work are shown in Table 1. The selection of the parameterizations was based on the operating forecast default settings from the Center of Atmospheric Sciences of the National Autonomous University of Mexico (López-Méndez, 2009; Taylor-Espinosa, 2009, 2014) and on standard parameterization schemes for tropical regions (Tewari et al., 2004; Gunwani and Mohan, 2017; Fonseca et al., 2019). We used three (one-

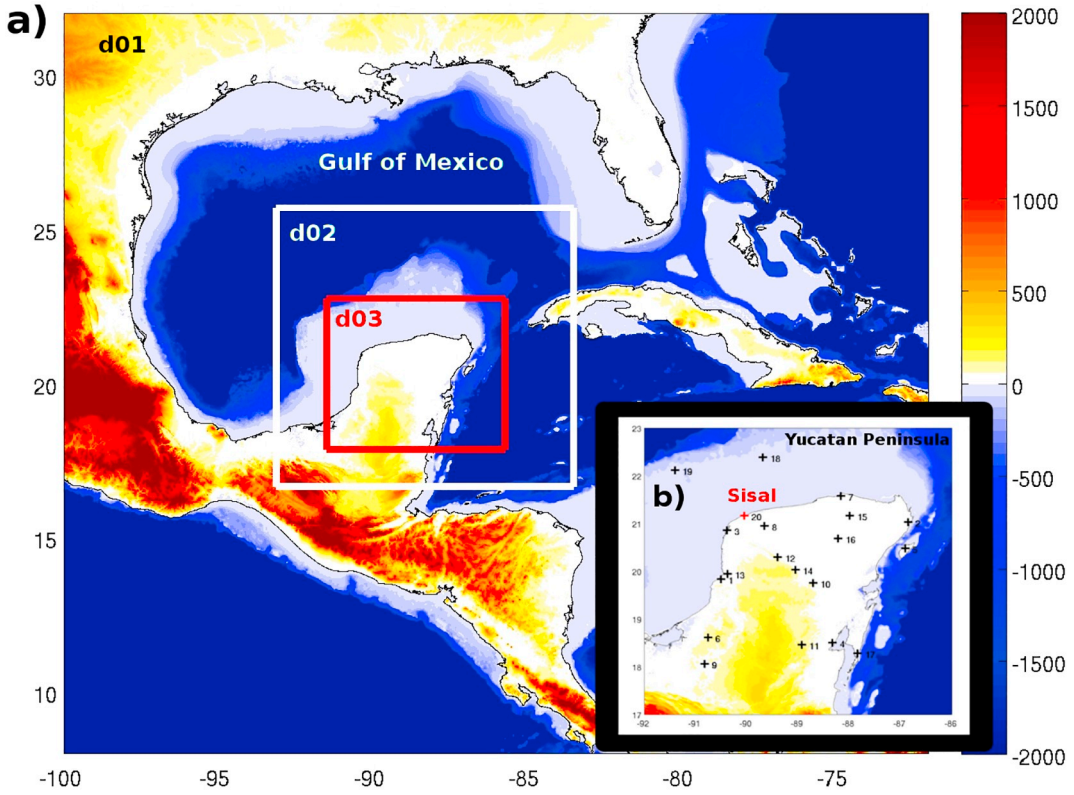

Fig. 1. Study area location. (a) Domains considered in the configuration of the WRF numerical model. (b) d03 from WRF domains, where the crosses indicate the meteorological stations location.

way) nested computational domains. The first domain (d01) has a 33 km horizontal grid resolution and includes the GoM, Caribbean Sea, part of the Atlantic, and part of the northeastern tropical Pacific. The second domain (d02) has a resolution of 11 km and includes the central GoM, part of the northwestern Caribbean Sea, and the YP. The third, and finest, domain (d03) has a 3.6 km resolution and covers the YP (Fig. 1). Thirty vertical levels in a log-normal distribution, with the top of the atmosphere fixed at 50 hPa were defined. For the initial and boundary conditions, the numerical model was initialized with the global atmospheric reanalysis database from ERA-Interim, produced by the European Center for Medium-Range Weather Forecasts (Uppala et al., 2011). This database describes the atmospheric state on a global scale, on a grid of 0.75° x 0.75°, with temporal resolution of 6-h (ECMWF, 2006) (Carvalho et al., 2014).

The model equations were integrated every 180 s, 60s, and 20s time-step for the d01, d02, and d03 domains, respectively. A 26-day simulation was performed (00,00 UTC March 24 to 21:00 UTC April 18, 2014) as hindcast mode, considering that the breezes are submesoscale phenomena that are better reproduced in a high-resolution simulation. The model outputs have a temporal resolution of 1-h for all three domains.

3.2.2. Model validation

The WRF model validation was done for the study period (00:00 UTC April 1st to 21:00 UTC April 12, 2014) using wind and temperature data from 20 sites (Fig. 1b). The meteorological stations are listed in Table 3. (further on in this section). The nearest model grid point was chosen for the comparison at each location. Previously a test comparing the model temperature at 2 m of the four nearest grid points and the value at the location obtained by a bilinear interpolation of the two stations in keys (Cayo Arenas and Isla Pérez) was performed. It was found that the average differences were less that 0.024 °C with a standard deviation of 0.018 °C and the average RMSE of all comparisons was 0.028 °C. Therefore, for the model output comparison against observations, we used the nearest grid point to each station of the d03 domain. Subsequently, time series were extracted for the wind direction and wind velocity components (u, v) at 10 m, and for the temperature at 2 m above the surface. Statistical analysis was done to assess the model results.

For wind speed and temperature, the correlation coefficient (CC), standard deviation (SD), root mean square error (RMSE), mean bias error (MBE), percent mean bias error (PMBE), and index of agreement (IA) were calculated (Robinson, 1957; Willmott, 1982; Davis et al.,

Table 1
WRF model configuration of the physics parameterizations used in this work.

Parameterizations	d01	d02	d03	Sources
Atmospheric Microphysics	WRF Single-Moment 3-class scheme			Hong et al. (2004)
Planetary Boundary Layer Scheme	Yonsei University Scheme (YSU)			Hong et al. (2006)
Land Surface Model	Unified Noah Land Surface Model			Tewari et al. (2004)
Surface Layer Physics	MM5 similarity based on Monin-Obukhov and Carslon-Boland			Dyer and Hicks (1970); Paulson (1970); Webb (1970); Zhang and Anthes (1982); Beljaars (1995)
Long wave radiation scheme	Rapid Radiative Transfer Model Scheme			Taubman et al. (1997)
Short wave radiation scheme	Dudhia Scheme			Dudhia (1989)
Cumulus Physics	Kain-Fritsch Scheme		Explicit	Kain (2004)

Table 2
Mathematical expressions of the model performance metrics used in the statistical analysis. **S** stands for simulated and **M** for measured data. Overbar indicates the average value.

Index	Mathematical expression	Index	Mathematical expression
RMSE	$=\left[\frac{1}{n}\sum_{i=1}^{n}(M_i - S_i)^2\right]^{1/2}$	MBE	$=\overline{S} - \overline{M}$
IA	$=1 - \frac{\sum_{i=1}^{n}(S_i - M_i)^2}{\sum_{i=1}^{n}(\mid S_i - \overline{M}\mid + \mid M_i - \overline{M}\mid)^2}$	PMBE	$=\frac{MBE}{\sum_{i=1}^{n}\mid M_i\mid} * 100$
MAPE	$=\frac{100}{n}\sum_{i=1}^{n}\left\lvert\frac{M_i - S_i}{M_i}\right\rvert$	CC	$=\frac{\sum_{i=1}^{n}(S_i - \overline{S})(M_i - \overline{M})}{[\sum_{i=1}^{n}(S_i - \overline{S})^2]^{1/2}[\sum_{i=1}^{n}(M_i - \overline{M})^2]^{1/2}}$
MVL	$=(x^2 + y^2)^{1/2}$, where $x = \frac{1}{n}\sum_{i=1}^{n}cos(\theta_i)$ and $y = \frac{1}{n}\sum_{i=1}^{n}sin(\theta_i)\theta_i$ is the corresponding angle		
CSD	$=(-2\log\overline{R})^{1/2}$ $[0,\infty]$ where $R = MVL$ is the resultant vector length		
MD	$=\begin{Bmatrix} arctan(y/x)\ \ if\ \ x \geq 0 \\ arctan(y/x) + \pi\ \ \text{if}\ \ x < 0 \\ undefined\ \ if\ \ MVL = 0 \end{Bmatrix}$	CCC	$=\frac{\sum_{i=1}^{n}sin(a_i - \overline{a})\,sin(b_i - \overline{b})}{\{\sum_{i=1}^{n}sin^2(a_i - \overline{a})\,sin^2(b_i - \overline{b})\}^{1/2}}$ where a and b are angular data, with angular means $\overline{a}$ and $\overline{b}$

Table 3
Statistical metrics (RMSE: root mean square error; PMBE: percent mean bias error; SD: standard deviation; CC: correlation coefficient; CSD: circular standard deviation; CCC: circular correlation coefficient) used to evaluate model performance for reproducing the wind speed (ms^{-1}) and direction (^{o}) at each of the 20 meteorological stations. Model validation was carried out for the study period (April 1–12). Model domain d03 data and measured data have a frequency of 1 h. Asterisk (*) indicates a significant correlation at the 95% confidence level. **S** stands for simulated data and **M** for measured data.

Meteorological station		Domain d03							
Name	No.	RMSE (ms^{-1})	PMBE (%)	SD (ms^{-1})		CC (ms^{-1})	CSD (^{o})		CCC (^{o})
				S	M		S	M	
Campeche	1	6.54	2.61	2.56	0.36	0.35	1.47	1.42	**0.55***
Cancún	2	4.38	1.28	1.56	0.33	**0.69***	0.95	0.99	**0.82***
Celestun	3	6.55	1.65	2.48	0.45	**0.49***	1.31	1.32	**0.78***
Chetumal	4	3.00	1.04	1.37	0.32	−0.10	0.93	0.91	0.09
Cozumel	5	7.13	4.62	1.08	0.49	0.30	0.88	0.89	**0.65***
Escárcega	6	3.06	1.88	1.21	0.31	**0.52***	1.01	1.04	**0.47***
Río Lagartos	7	6.47	1.96	1.72	0.53	0.10	0.92	0.98	**0.76***
Mérida	8	3.10	1.09	1.34	0.33	**0.74***	0.96	1.10	**0.74***
Monclova	9	2.78	1.68	1.32	0.27	**0.68***	1.11	1.18	0.22
J.M. Morelos	10	3.00	2.05	1.21	0.32	**0.79***	0.96	1.00	0.40
Nicolas Bravo	11	2.73	1.70	1.32	0.31	**0.76***	0.99	1.35	−0.13
Oxkutzcab	12	3.88	2.32	1.49	0.32	**0.75***	0.95	0.90	0.16
Los Petenes	13	4.40	2.37	1.92	0.35	**0.56***	1.34	1.25	−0.05
Tantaquin	14	2.62	0.99	1.34	0.57	**0.71***	1.00	1.06	0.28
Tizimin	15	3.35	1.92	1.41	0.55	**0.87***	0.95	0.99	**0.64***
Valladolid	16	3.08	1.47	1.34	0.33	**0.85***	0.97	0.90	**0.58***
Xcalak	17	2.74	0.286	1.40	0.99	0.06	0.81	0.77	**0.64***
Isla Pérez	18	1.49	−0.073	1.69	1.46	**0.68***	0.45	0.39	**0.88***
Cayo Arenas	19	1.69	0.120	2.18	2.35	**0.74***	0.53	0.01	**0.74***
Sisal	20	2.53	0.004	2.34	2.96	**0.56***	0.89	0.94	**0.83***

1985; Legates and Mccabe, 2013). Some authors recommend the use of mean absolute percent error (MAPE) for validation purposes (e.g., Chai and Draxler, 2014), which is a scale-independent measure bounded by the weakest wind speeds and lowest temperatures (Goodwin and Lawton, 1999; Fernández-González et al., 2017, 2018). MAPE reduces the influence of extremely large (northerly winds) and/or small (breezes) values, and/or outliers, which can be undesirable during strong/weak wind episodes. Thus, MAPE values were also calculated in this study. Furthermore, circular statistics, including the circular correlation coefficient (CCC), circular standard deviation (CSD), mean vector length (MVL) and mean direction (MD) (Fisher and Lee, 1983; Jammalamadaka and Sarma, 1988; Davis, 2003; Mardia and Jupp, 2008; Carvalho et al., 2012), were also employed to assess model performance regarding the wind direction (metrics that gives a linear relationship between angular variables). Values of the CC and CCC were statistically significant, with a confidence level of 95%, in 70% and 60% of the stations, respectively. The mathematical expressions of the performance metrics used in the statistical analysis are shown in Table 2.

The numerical model satisfactorily reproduces the observed daily cycle of wind speed and direction for the simulation period based on the CC and CCC values (Sepp and Jaagus, 2002; Asuero et al., 2006; Senatore et al., 2014; Bolgiani et al., 2018). With respect to the wind speed, the averaged metrics considering all stations showed an MBE of 3.21 ms^{-1} and a PMBE of 1.55%, the latter indicating an overestimation in a low-magnitude percentage of the wind speed. A mean IA value of 0.29 was obtained, and although the error is relatively large (averaged RMSE = 3.71 ms^{-1}), indicates is not a systematic error. Differences in the SD between the observed and simulated wind speed suggest that the numerical model reproduces the diurnal variability of the measured data with a mean overestimation of approximately 0.92 ms^{-1}. On the other hand, for the wind direction, the circular statistics showed a mean CSD of 0.98°. Regarding the measure of circular variance calculated with the MVL, which shows the group of angles of the MD, the values were almost equal for both observed and simulated data, indicating an acceptable performance for wind direction variability. However, the averaged MD values showed a difference in wind direction of 62.8° between measured and simulated results. Such results imply an important direction change in the model data during few time periods (less than 24 h) for some stations (e.g., stations 1, 2, 6, 8, and 16). Based on a previous analysis of the wind components, this aforementioned direction change, can be associated with the wind meridional component.

Table 4
Magnitude of the semi-major (SMA) and -minor (SMI) axes of the ellipses adjusted to the wind data of the 20 meteorological stations, both for **S**imulated and **M**easured data during the study period (April 1–12).

Meteorological station		Domain d03			
Name	No.	SMA		SMI	
		S	M	S	M
Campeche	1	3.12	0.15	1.89	0.05
Cancún	2	0.97	1.66	0.59	0.78
Celestun	3	2.06	1.10	2.00	1.01
Chetumal	4	1.98	0.54	1.01	0.53
Cozumel	5	0.69	0.50	0.49	0.15
Escárcega	6	1.00	0.51	0.30	0.17
Río Lagartos	7	1.50	1.45	0.70	0.54
Mérida	8	0.38	0.15	0.17	0.03
Monclova	9	1.03	0.95	0.10	0.42
J.M. Morelos	10	0.80	0.60	0.53	0.05
Nicolas Bravo	11	1.28	0.68	0.46	0.34
Oxkutzcab	12	0.52	0.57	0.15	0.21
Los Petenes	13	2.86	0.15	1.63	0.03
Tantaquin	14	0.44	0.38	0.28	0.35
Tizimin	15	0.66	0.69	0.58	0.12
Valladolid	16	0.67	0.12	0.64	0.12
Xcalak	17	1.64	1.34	1.52	0.20
Isla Pérez	18	0.73	4.28	0.44	0.15
Cayo Arenas	19	2.01	3.86	0.96	4.20
Sisal	20	1.64	2.71	1.44	0.66

Table 5
Characteristic parameters of the adjusted ellipses and explained variance of the diurnal signal of each wind component (u_{svd}, v_{svd}), for the breeze events and the CS event. Gyre indicates the wind direction of rotation (**C**yclonic: anti-clockwise / **A**nticyclonic: clockwise). Magnitude of the semi-major (SMA) and -minor (SMI) axes, the minimum angle between the semi-major axis and the east direction (Φ), eccentricity (Ec), and time when winds were aligned with the major axis of the ellipse (t_0).

Event	Gyre	SMA (ms^{-1})	SMI (ms^{-1})	Φ (°)	Ec	t_0 (hr)	u_{svd}	v_{svd}
Breeze	A	3.92	1.91	105.72	0.87	0.49	0.89	0.75
Cold Surge	A	2.66	1.12	69.57	0.90	−0.73	0.63	0.87

Concerning temperature, the model correctly reproduces the daily cycle; however, the MBE showed that the model underestimates the measured values up to 5.5 °C. This value fits in the intervals already reported in previous studies using the WRF model (e.g., Papanastasiou et al., 2010). The PMBE value obtained for the temperature was of −0.09%, which suggests an almost accurate simulation (Harmel et al., 2007; Carvalho et al., 2014). Prior modeling studies employing the WRF model have shown that one of the leading causes of the over- and underestimated values in a simulation, are ascribed to either the surface parameterization associated with the sea-land temperature gradient (Papanastasiou et al., 2010; Carvalho et al., 2012; Li and Chao, 2016) or to the smoothing terrain characteristics (Carvalho et al., 2014).

With respect to the coastal station (Station 20), located near the Sisal Port, the statistic indexes show a CC of 0.56 and 0.74 for the wind speed and the temperature, a MAPE of 35.35% and 20.43%, a PMBE of 0.004% and 0.03%, and a mean SD of 2.34 ms^{-1} and 2.8 ° C, respectively. The IA obtained value for wind speed was 0.99, suggesting a high coincidence with measured data, while obtaining a value of 0.47 for temperature. Moreover, for the wind direction, the results showed a CCC of 0.83, a MVL of 0.035° for measured and 0.011° for simulated data, being sufficiently close MD values of 168.1° and 157.5°, respectively. Thus, model simulation satisfactorily reproduces the diurnal variability of wind speed and direction for Sisal, as reported in previous studies. For instance, Fita et al. (2013) found that ERA-Interim database produces the most accurate 10 m wind WRF estimation, in terms of wind variability. They obtained a CC that oscillates between 0.69 and 0.8 and a RMSE between 2 and 2.8 ms^{-1}, intervals which depend on the model parameterization schemes used by the authors. Another case concerning the wind speed is reported by Carvalho et al. (2012), who validated the 10 m wind data from WRF model simulations, obtaining values of the calculated metrics similar to those obtained in this study (RMSE = 2.43 ms^{-1}, BIAS = -1.09 ms^{-1}). Concerning temperature, an example is the work of Papanastasiou et al. (2010), who validated WRF model simulations under different numerical and physical options. In general, they obtained for the near-surface air temperature a RMSE between 1.1 and 2.3 °C, supported by an IA of 0.7, reporting that in some cases, the resulting differences of temperature were more than 3 °C.

3.3. Data analysis

The validated WRF model results were employed for the analysis of the wind diurnal signal. The diurnal horizontal movement of the near-surface coastal wind associated with breezes can be described, according to linear theory, with an ellipse (Haurwitz, 1947; Schmidt, 1947). Therefore, while combining the wind direction and wind speed information, we obtained time series for the zonal (u) and meridional (v) wind components. Subsequently, the zonal and meridional wind components were adjusted to an elliptical signal by means of the least-squares method. Moreover, a harmonic analysis was performed to obtain the explained variance of the diurnal signal and the diurnal component (24 h frequency) of the wind speed. The elliptical signal was fitted as follows:

$$u_i = A + Bcos(\omega t_i) + Csin(\omega t_i);\ v_i = D + Ecos(\omega t_i) + Fsin(\omega t_i) \quad (1)$$

where (A, D) (u_0, v_0) are constants related to the non-diurnal wind component, (B, E) (u_1, v_1) and (C, F) (u_2, v_2) allow to obtain information about tilt, rotation, and magnitude of the semi-axes, and ω represents the diurnal frequency ($2\pi/24hrs$). The system of linear equations was solved using the Singular Value Decomposition (SVD) method to calculate the values of the coefficients A to F (Golub and Reinsch, 1971; Lawson and Hanson, 1974). The coefficient values for u and v were obtained for the whole signal, from which the magnitude of the semi-axes, ellipse tilt (the semi-major axis angle with respect to the east), and the time at which the wind is aligned with the major axis of the ellipse, were calculated. Subsequently, the hourly averages of the identified breeze events were obtained and compared with the calculated ellipse. To evaluate the best-fit ellipse, the RMSE and MVL metrics were calculated (Fisher, 1995; Mardia and Jupp, 2008). Therefore, MVL is a measure of concentration, invariant under rotation. This analysis was carried out for both the breeze events and the CS event occurring during the study period. The RMSE was 0.12 and 0.10 m s^{-1}, respectively. The MVL metric showed that for the breeze events over 74% of the diurnal signal was represented by the adjusted ellipse, but only 55% for the CS event. The ellipse characteristic parameters, given by the magnitude of the semi-major (SMA) and -minor (SMI) axes (Table 4), the minimum angle between the semi-major axis and the east direction (Φ), the eccentricity (Ec), and the time when winds were aligned with the major axis of the ellipse (t_0), were also obtained. Finally, Hovmöller (HM) diagrams along two transects, zonal and meridional, were constructed to describe the evolution through time.

4. Results and discussion

Breeze conditions mostly dominated wind dynamics in the study area during the analyzed period (i.e., 1–12 April 2014), whereas a high-pressure system persisted at the north of the GoM most of the time and arrived at the study area on April 8th. This high-pressure system then moved northeastward towards the Atlantic. On the other hand, two high-pressure systems remained partially stationary over continental Mexico, one between the Sierra Madre Oriental and the Sierra Madre Occidental (west of the YP) and the other one over the state of Chiapas,

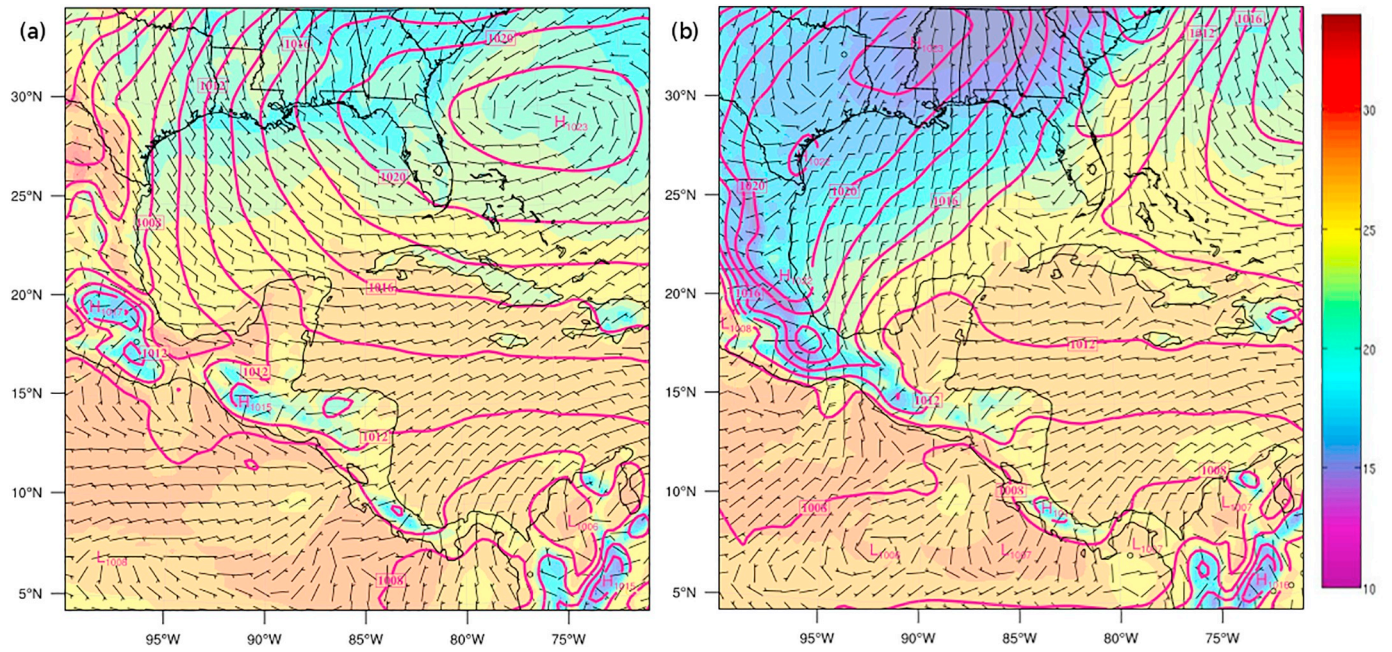

Fig. 2. WRF-d01 surface synoptic maps for (a) breeze conditions (April 6, 2014 at 00:00 UTC [April 5, 2014 at 18:00 h LT]) and (b) CS conditions (April 9, 2014 at 00:00 UTC [April 8, 2014 at 18:00 h LT]). The magenta lines are contours of sea-level pressure (hPa), the filled-color contours represent the 2 m air temperature (°C), and the barbs the wind magnitude ($m\,s^{-1}$) and direction. (For interpretation of the references to color in this figure legend, the reader is referred to the web version of this article.)

near the border with Guatemala (south of the YP) (Fig. 2a). Both the wind intensity and direction remained relatively constant, with an average magnitude of 7.6 ms^{-1}. The weak pressure gradient over the YP favored the development of local circulations such as breezes (Li and Chao, 2016).

4.1. Breeze diurnal variability

Breeze variability is influenced by both synoptic and local wind variability. The numerical results show that the meridional component of the wind (v) has a greater influence during breeze events. When obtaining the wind diurnal frequency from the model data, the adjusted ellipse shows an anticyclonic gyre associated with the Coriolis force (Fig. 3c) (Neumann, 1977, 1984; Alpert et al., 1984), with a maximum SMA of 3.92 ms^{-1}, almost twice the amplitude of the global diurnal signal (SMA = 2 ms^{-1}) reported by Gille et al. (2005). This feature is associated with the direction of the synoptic-scale wind relative to the coastline position. The characteristic parameters of the adjusted ellipses and the explained variance of the diurnal signal of the wind components are presented in Table 5. Maximum wind intensity was reached on average between 21:00 and 22:00 UTC for the sea breeze and between 10:00 and 11:00 UTC for the land breeze, corresponding to 15:00 and 16:00 h LT and 04:00 and 05:00 h LT, respectively (Table 5, Fig. 3a). Nevertheless, the time of the wind peak may change depending on the month and season (Manobianco et al., 2005; Taylor-Espinosa, 2009).

A characteristic of the diurnal component is the eccentricity of its associated ellipse, which in the case of Sisal was 0.87 (Table 5). Although the signal has a large amplitude, it is not determinant for the ellipse to be more eccentric, since eccentricities close to one are associated with an abrupt or sudden change in wind direction due to friction and differential heating of the thermal forcing, and are also related to the non-diurnal wind component (Neumann, 1984; Alpert et al., 1984; Papanastasiou et al., 2010; Giffen et al., 2012). With low atmospheric synoptic-scale variability (tropical storms or low-pressure systems) modulating the region and a weak presence or non-northerly winds, the SMA of the ellipse has a tilt of 106° with respect to the east. In this study case, the SMA tilt is due to the influence of the easterly winds. The change in the wind direction, the diurnal signal amplitude, and the hour of the day at which the largest amplitude in breeze signal is observed are associated with other meteorological variables such as temperature and relative humidity (Fig. 4). In the case of temperature, a thermal gradient with a diurnal variation is generated due to differential heating between sea-land surfaces (Martin and Pielke, 1983; Miller et al., 2003; Li and Chao, 2016; Kishtawal et al., 2016). The air temperature variability under breeze conditions during the study period, considering the nine breeze events identified from April 1st to 7 and April 11 to 12, oscillates between 18.3 °C and 30.5 °C, depending on the mesoscale atmospheric conditions (Fig. 4c). In the case of relative humidity, it oscillates from 32% to 97% (Fig. 4d). Under average breeze conditions, the difference in diurnal change of the relative humidity is 65%. Similar to temperature, the relative humidity is also modulated by mesoscale dynamics but also by local dynamics, depending on the properties (wet-dry) of the air mass (Challa et al., 2009). These results are consistent with those of Yan and Anthes (1988) and with the findings of Kishtawal et al. (2016), who determined that one of the essential pre-conditions for breeze formation in coastal areas is the difference in humidity content of the air masses over land (hot and dry air) and the sea (cold and humid air). When these air masses with different properties are advected, moisture accumulates in the lower atmosphere, which, in combination with intense solar heating, creates a potential instability that causes the breezes (Van Delden, 2000; Day et al., 2010; Hu and Xue, 2015). The associated relative humidity gradient in the area causes the wind to rotate with an abrupt change in its direction. When the temperature gradient is large, the wind progression, either towards the land (sea breeze) or towards the sea (land breeze), moves air masses with properties different from those of the region they arrive. This leads to a change in humidity and hence in pressure. Furthermore, the diurnal variation in atmospheric pressure is attenuated by the semi-diurnal and diurnal breeze variations (Fig. 4e).

The thermal gradient is one of the main factors that generate the breeze (Martin and Pielke, 1983; Miller et al., 2003; Suresh, 2007; Li and Chao, 2016; Kishtawal et al., 2016), making the diurnal wind component to be mainly oriented perpendicularly to the coastline and

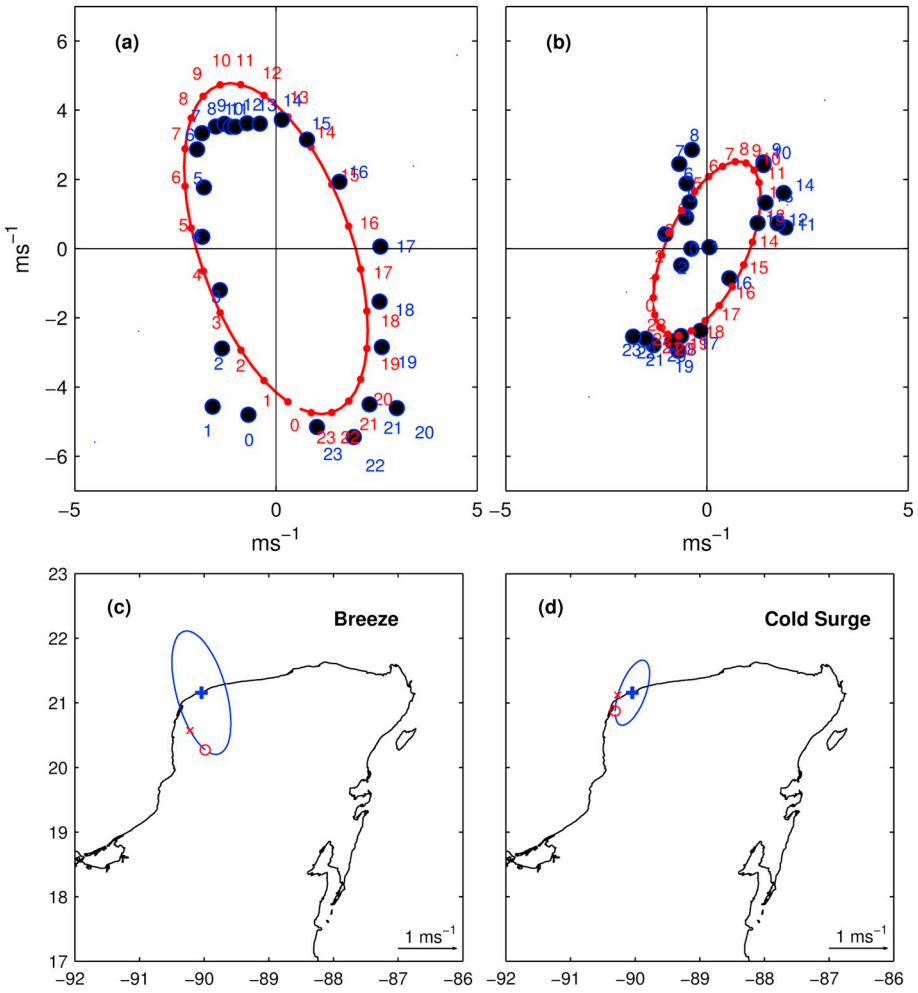

Fig. 3. WRF-d03 hourly average wind speed (black dots) and ellipse adjusted by SVD (red dots) for (a) the breeze events (April 1st to April 7 and April 11 to April 12) and (b) the CS event (April 8th to April 10). The maps in (c) and (d) show the ellipses calculated for each case, where the blue cross in the center indicates the location of Sisal, Yuc., (21° 09′ 56.20" N, 90° 02′ 26.44" W), the red circle the wind at 00:00 h UTC and the red cross the wind at 06:00 h UTC. (For interpretation of the references to color in this figure legend, the reader is referred to the web version of this article.)

be aligned with the sea-land temperature gradient as expected in tropical latitudes. To analyze the sea-land temperature differences, the maximum and minimum daily data averaged from April 1 to April 12 were compared between Isla Pérez (located northeast of Sisal at 22° 23′ 03" N, 89° 40′ 54" W) and Sisal. The absolute differences in maximum and minimum air temperature near the surface between the two locations (Fig. 5a) and the SMA of the ellipse calculated at each location (Fig. 5b) were obtained. Temperature differences are smaller when the synoptic-scale atmospheric conditions modify the local dynamics (April 9th in Fig. 5). Even with the arrival of the CS a small difference between sea-land temperature was found (Fig. 4c), enough to make the diurnal signal prevail. Thus, the SMA is mainly dominated by temperature rather than by wind magnitude, and as a result, the diurnal signal persists. The persistence of the breeze phenomenon will be described in the next sections.

4.1.1. Sea and land breeze winds

Figs. 6 and 7 show 3-hourly wind maps for the 5th of April 2014, which are representative of the average conditions of breezes. The 24-h UTC corresponding to this day were selected, considering that breeze dynamics begin after mid-day. Fig. 6 shows that the YP has a relatively uniform temperature at dawn (12:00 h UTC or 06:00 h local time [LT]), with lower temperatures compared to sea. At 18:00 h UTC (12:00 h LT) the temperature difference between sea and land is above 5.4 °C, being the land temperatures higher. The differential heating causes the wind direction to change drastically in only a few hours and the sea breeze winds become intense enough to reduce the effect of the mean wind (easterly wind). The breeze front steadily progresses inland from 21:00 h UTC to 03:00 h UTC of the next day (15:00 h to 21:00 h LT). The convergence that forms with the easterly wind (breeze front) is observed along the western coast of the YP (Fig. 7). The results obtained by analyzing the time series along the meridional transect show a pressure anomaly caused by the temperature difference at the sea-land interface. In the HM diagram (Fig. 8), the wind component v converges inland when warming is maximum (Fig. 8a), between 18:00 and 21:00 h UTC (12:00 and 15:00 h LT) and displaces southward (Fig. 8b and c). This displacement is associated with the strengthening of the pressure differences and hence the wind direction change induces a convergence that causes the breeze front (Fig. 7) (Gentry and Moore, 1954; Challa et al., 2009; Papanastasiou et al., 2010; Birch et al., 2015). The pressure anomaly formed can be considered as a density current (Manobianco et al., 2005; van der Wiel et al., 2017) that determines the widening of the breeze cell (breeze circulation formed by the vertical and horizontal displacement of the land-sea air masses, according to Miller et al., 2003; Li and Chao, 2016) as the winds intensify within the circulation cell, limit at which an offshore divergence is formed (Martin and Pielke, 1983; Atkinson and Zhang, 1996; Gahmberg et al., 2010; Papanastasiou et al., 2010). When the sea breeze enters, the land temperature is modified and the thermal gradient decreases, causing the breeze cell to weaken.

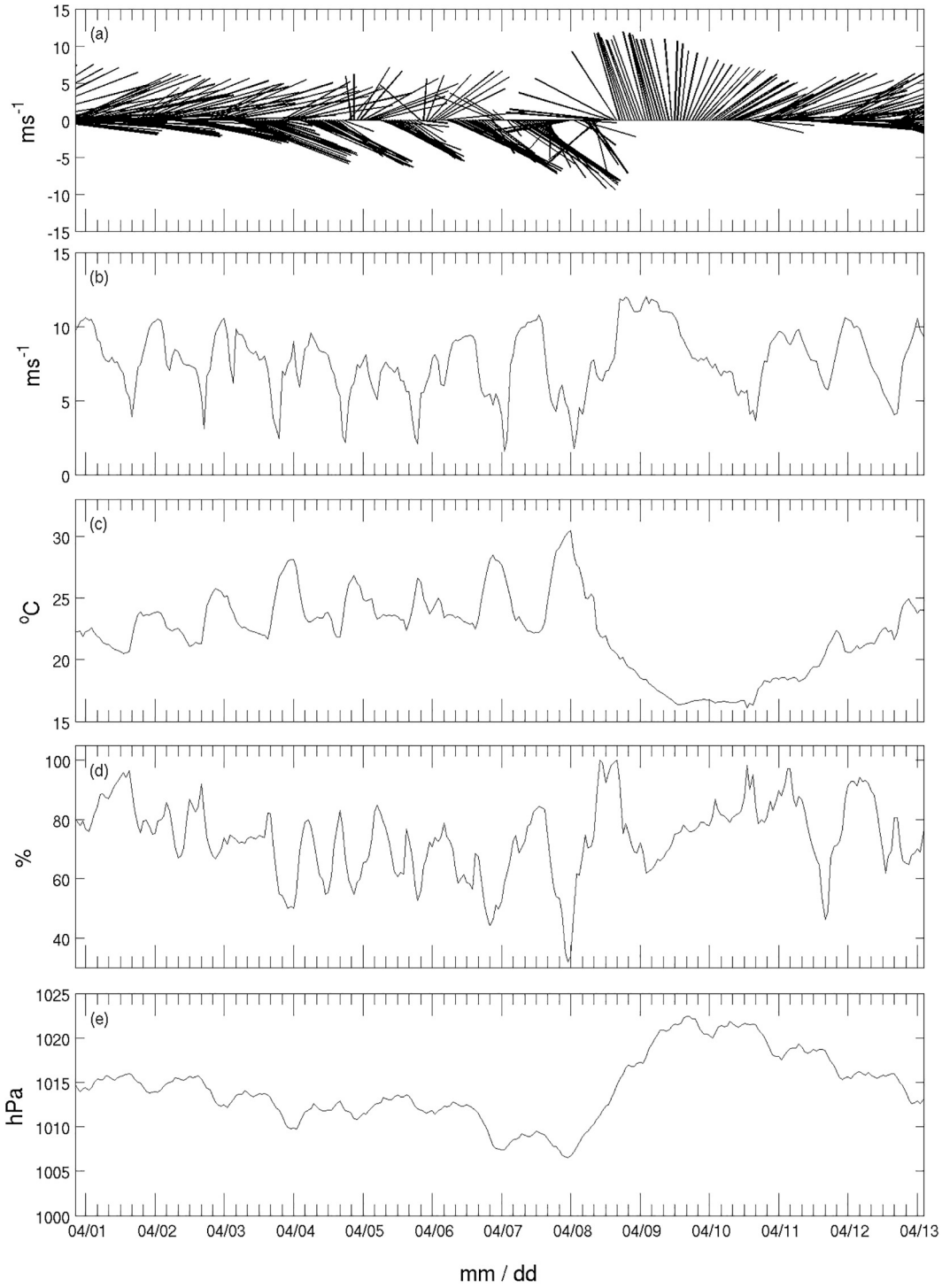

Fig. 4. Time series of meteorological variables from WRF-d03 in Sisal, Yuc., from April 1–12, 2014. (a) Wind direction and magnitude (feather diagram), (b) wind speed (ms^{-1}), (c) air temperature (°C), (d) relative humidity (%), and (e) mean sea-level pressure (hPa).

Land cooling begins after 00:00 h UTC (18:00 h LT), which reduces the sea breeze effect and reverses direction after approximately three hours (03:00 h UTC, 21:00 h LT), resulting in a land breeze. The land breeze presents the same direction as the easterly wind, so that an increase in the intensity of the zonal component is observed propagating towards the ocean. The maximum land breeze then coincides with the minimum temperature gradient, when the land temperature decreases more than 10 °C (12:00 h UTC, 06:00 h LT) (Fig. 6). A reduction in the intensity of the sea breeze, while it penetrates and the temperature gradient reduces, contributes to the development of the land breeze. When the temperature rises over land, the breeze cell strengthens and the mean wind appears uniform and steady over the YP (Fig. 7). The land breeze and its influence on the adjacent atmosphere can be extended more than 100 km offshore, consistent with remote sensing observations (e.g., Gille et al., 2005).

Analysis of the numerical results showed an important asymmetry between the sea and land breezes. In both cases, a convergence zone was formed and a divergence zone developed as a product of the breeze front. Throughout the duration of the sea breeze, the meridional wind component becomes more dominant, penetrating landward. A well-

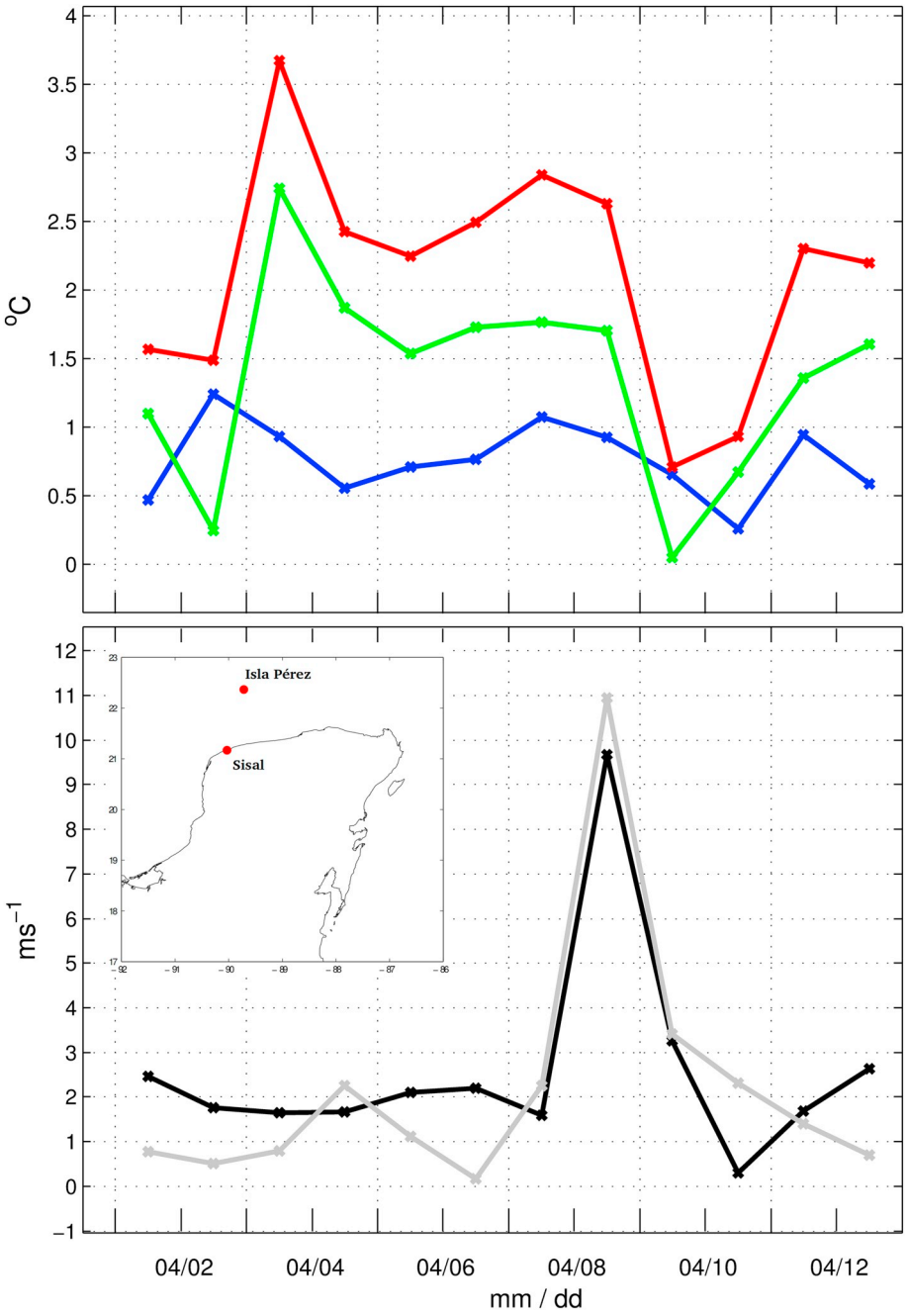

Fig. 5. (a) Differences in daily average minimum and maximum temperatures between Isla Pérez and Sisal from WRF-d03. The red line is the maximum temperature difference, the blue line is the minimum temperature difference, the green line the difference between the maximum and minimum temperature difference (red minus blue line) and (b) represents the amplitude of the SMA of the ellipse calculated for Sisal (black line) and Isla Pérez (gray line). (For interpretation of the references to color in this figure legend, the reader is referred to the web version of this article.)

defined sea breeze front is generated by the intensity of the opposing wind (easterly winds), causing a wind intensification behind the front. On the other hand, the convergence zones intensify the effect of the land breeze, which penetrates further offshore (Figs. 6 and 7).

4.1.2. Flow field generated by breezes

Sea breeze winds travel more than 100 km from the ocean to the coast. Fig. 7 shows that the sea breeze winds are more intense in the ocean ($> 8\,m\,s^{-1}$), and during afternoon (21:00–03:00 h UTC, 15:00–21:00 h LT) move inland with speeds over $10\,m\,s^{-1}$ and hence they are not limited to the coastal area. Therefore, the change in wind intensity will depend on the direction of the mean wind (opposite to the direction of the sea breeze) and the thermal gradient (Leopold, 1949; Gentry and Moore, 1954; Carvalho et al., 2014; Hughes and Veron, 2018) which causes the wind to decrease its intensity at some times during the day. The thermal contrast in the area is enhanced by the high solar radiation in the region and its considerable variability throughout the day. The diurnal range in temperature over the land surface exceeds 15 °C. Moreover, the extension of the breeze is limited by the friction effect of the surface. Therefore, the maximum wind speed is reached when the thermal gradient begins to decrease (Fig. 9a; Miller et al., 2003), and when the mean easterly and southeasterly winds are weak. According to Estoque (1962), more intense vertical movements are observed in zones where this thermal difference is minimal. The results of Martin and Pielke (1983) suggested that in a heating surface, the advection of the air mass in motion reduces the horizontal scale of the

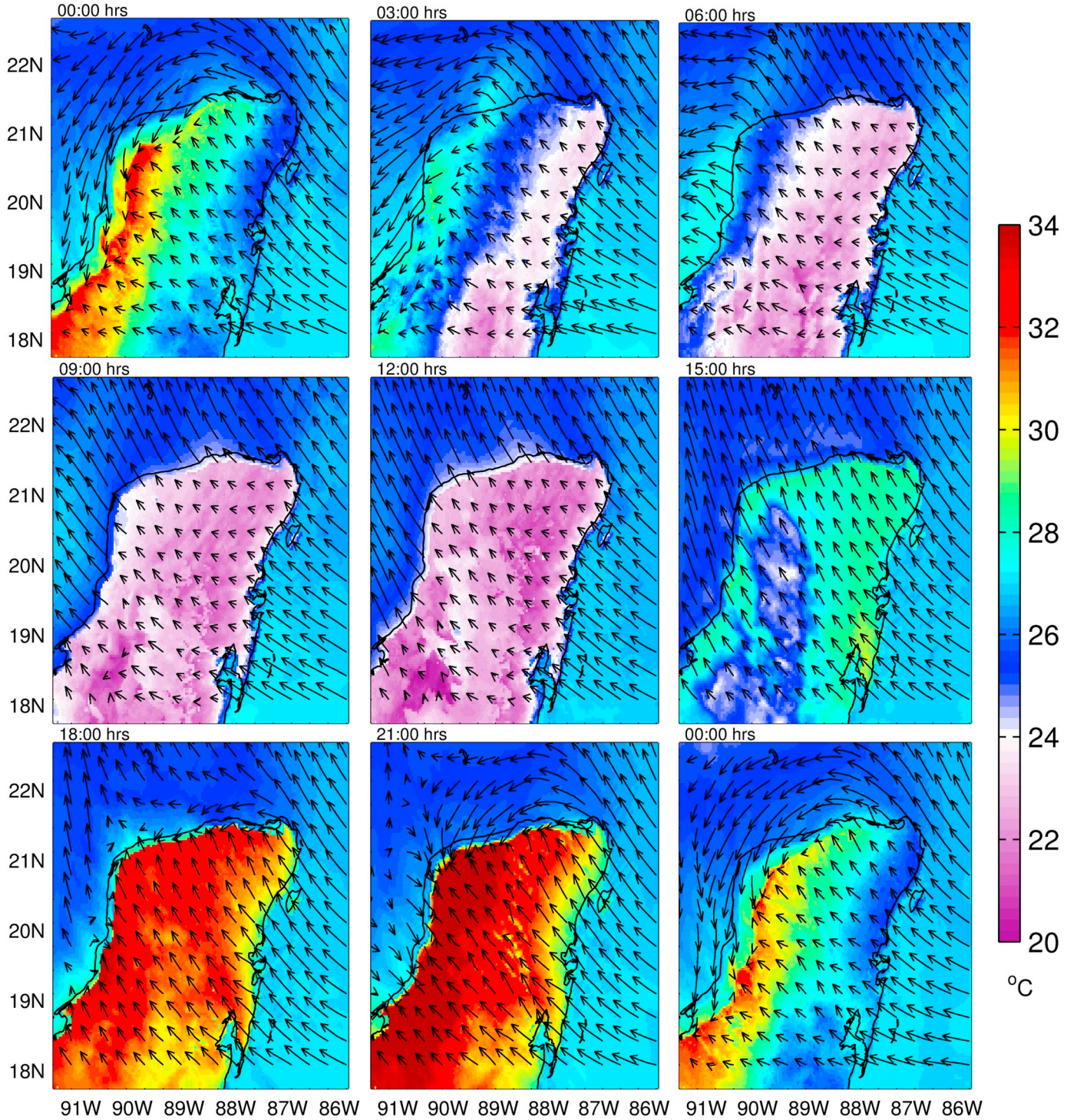

Fig. 6. Model-simulated horizontal wind field at 10 m (arrows) for a typical case of a breeze (from the d03 domain) on April 5, 2014. The maps also show the temperature at 2 m (background color). The maps have a time interval of three hrs from April 5 at 00:00 h UTC to April 6 at 00:00 h UTC, which corresponds to April 4 at 18:00 h LT to April 5 at 18:00 h LT.

circulation in low atmosphere levels, which combines with the friction effect. In the case of the land breeze, the surface friction over the ocean is less than overland; therefore, the progression of the offshore wind extends over a larger area (Fig. 8) (Stephan et al., 1999; Suresh, 2007). The HM diagram of a zonal transect in the study region (Fig. 9) shows that the maximum meridional component occurred 6 h after having presented the most intense winds that took place along the breeze front, which due to the effect of the mean wind, were displaced southwest. In this case the zonal component is almost imperceptible (Fig. 9b and c).

It must be considered that in these results, the period analyzed coincides with the maximum amplitude events of the observed signal (Manobianco et al., 2005; Azorin-Molina et al., 2011; Taylor-Espinosa, 2014). This maximum is not constant over time, as it presents a seasonal and annual variability (Manobianco et al., 2005; Srinivas et al., 2006; Taylor-Espinosa, 2009; Azorin-Molina et al., 2011; Giffen et al., 2012).

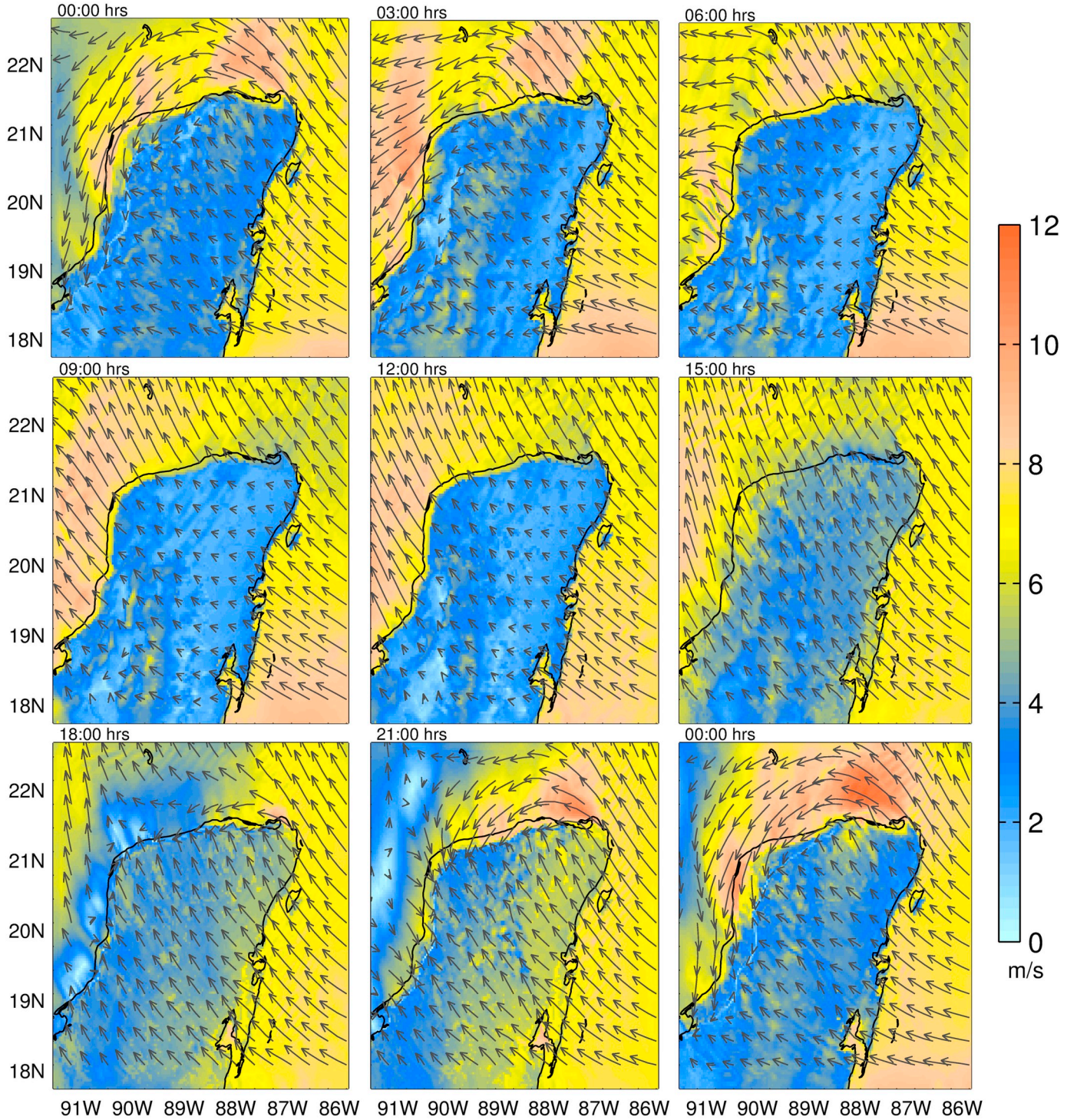

Fig. 7. Model-simulated horizontal wind field at 10 m (arrows) for a typical case of a breeze (from the d03 domain) on April 5, 2014. The maps also show the wind magnitude (background color). The maps have a time interval of three hrs from April 5 at 00:00 h UTC to April 6 at 00:00 h UTC, which corresponds to April 4 at 18:00 h LT to April 5 at 18:00 h LT.

4.2. Cold surge effect on breeze dynamics

Synoptic-scale events can modify breeze characteristics. A CS event reached the study area on April 8th with sustained winds of 12 ms^{-1}. This front arrived at the GoM associated with three high-pressure systems located on the continent (see Fig. 2b), and caused changes in the meteorological variables (see Fig. 4c-4d). However, the local atmosphere responded approximately 48-h before the CS arrival, called the pre-front period. During this pre-front period, the temperature had an increasing trend (Fig. 4c), while there was a fall in relative humidity (Fig. 4d) and mean sea-level pressure (Fig. 4e) regarding the previously observed variability.

During the passage of the CS, the wind speed exceeded 12 ms^{-1} (Fig. 4b), temperature decreased by around 9 °C (Fig. 4c), relative humidity increased to 100% (Fig. 4d), and subsequently, the pressure increased to exceed 1020 hPa (Fig. 4e). This CS event is considered typical since its characteristics are observed in approximately 32% of the CS events, according to the wind analysis of López-Méndez (2009).

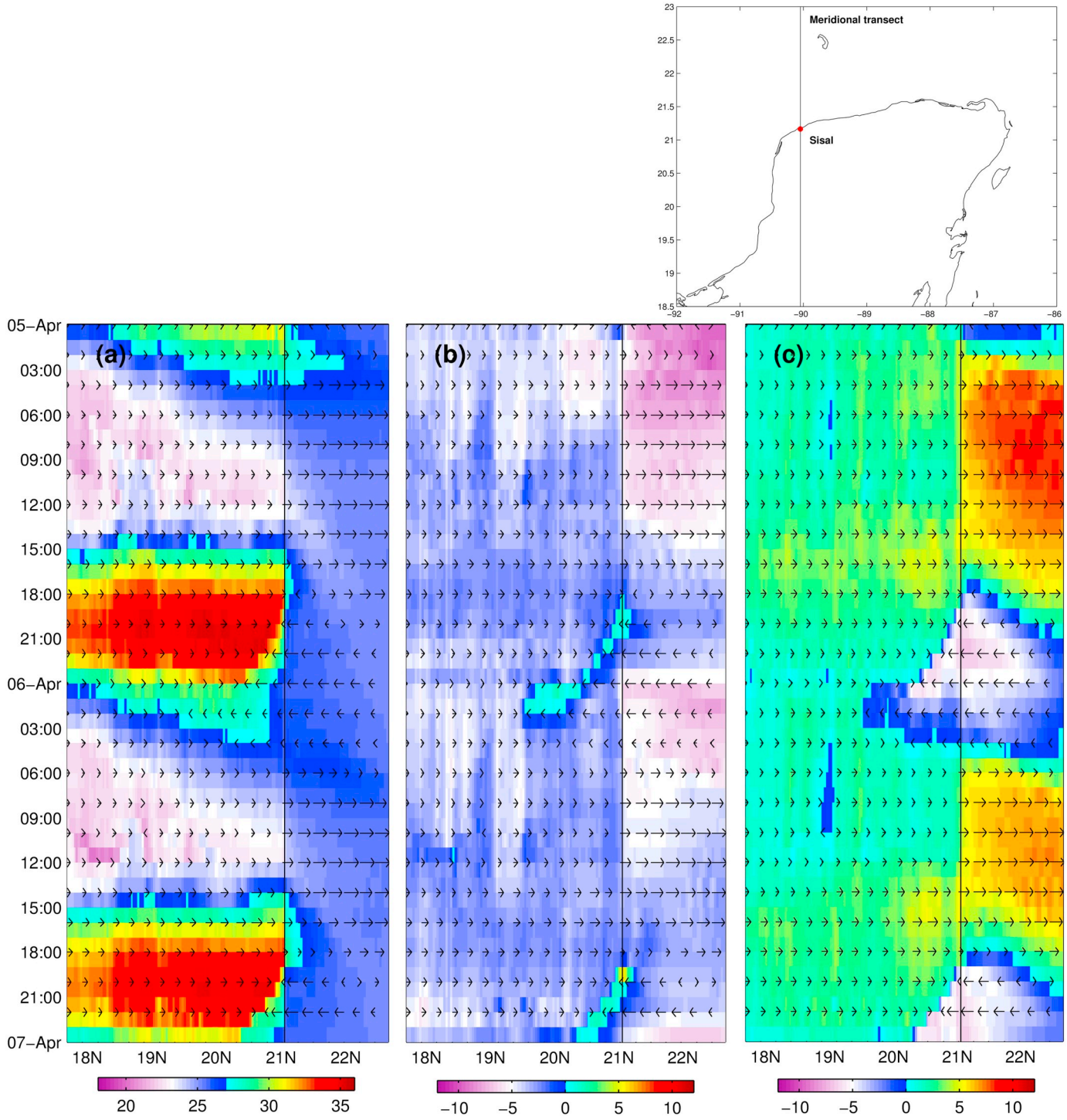

Fig. 8. Hovmöller diagram from d03 domain data, for a typical case of breeze. Meridional transect from April 5 at 00:00 h UTC to April 7 at 00:00 h UTC, which corresponds to April 4 at 18:00 h LT to April 6 at 18:00 h LT. The black line indicates the latitudinal position of Sisal (21° 09′ 56.20" N). (a) Air temperature at 2 m (°C), (b) zonal wind component *u* at 10 m ($m\,s^{-1}$), and (c) meridional wind component *v* at 10 m ($m\,s^{-1}$). The arrows represent the *v* component.

Considering the generated wave energy in the GoM, this CS corresponds to a Type III event, according to the classification of Appendini et al. (2018). Type III events represent approximately 16% of the CSs crossing the GoM, and they follow the Type II events as the most energetic with respect to the power of the generated waves, although similar or slightly milder than the Type I events around the YP.

Although the feather plot (Fig. 4a) shows that during the CS the breeze phenomenon does not develop, the analysis of the wind diurnal component showed the presence of a low diurnal signal modulation. Fig. 3b and d show the adjustment of the ellipse for the days of the CS event (April 8 to 10), indicating that the meridional wind component is predominant during the event. With the CS arrival, the elliptical signal has an anticyclonic gyre (Fig. 3d) with a maximum SMA of 2.66 ms^{-1} and -0.73 h lag. Maximum diurnal wind intensity during the CS was reached on average between 21:00 and 22:00 h UTC for the sea breeze and between 09:00 and 10:00 UTC for the land breeze, corresponding to 15:00 and 16:00 h LT and 03:00 and 04:00 h LT, respectively (Table 5, Fig. 3b). The ellipse eccentricity is 0.90, which indicates an

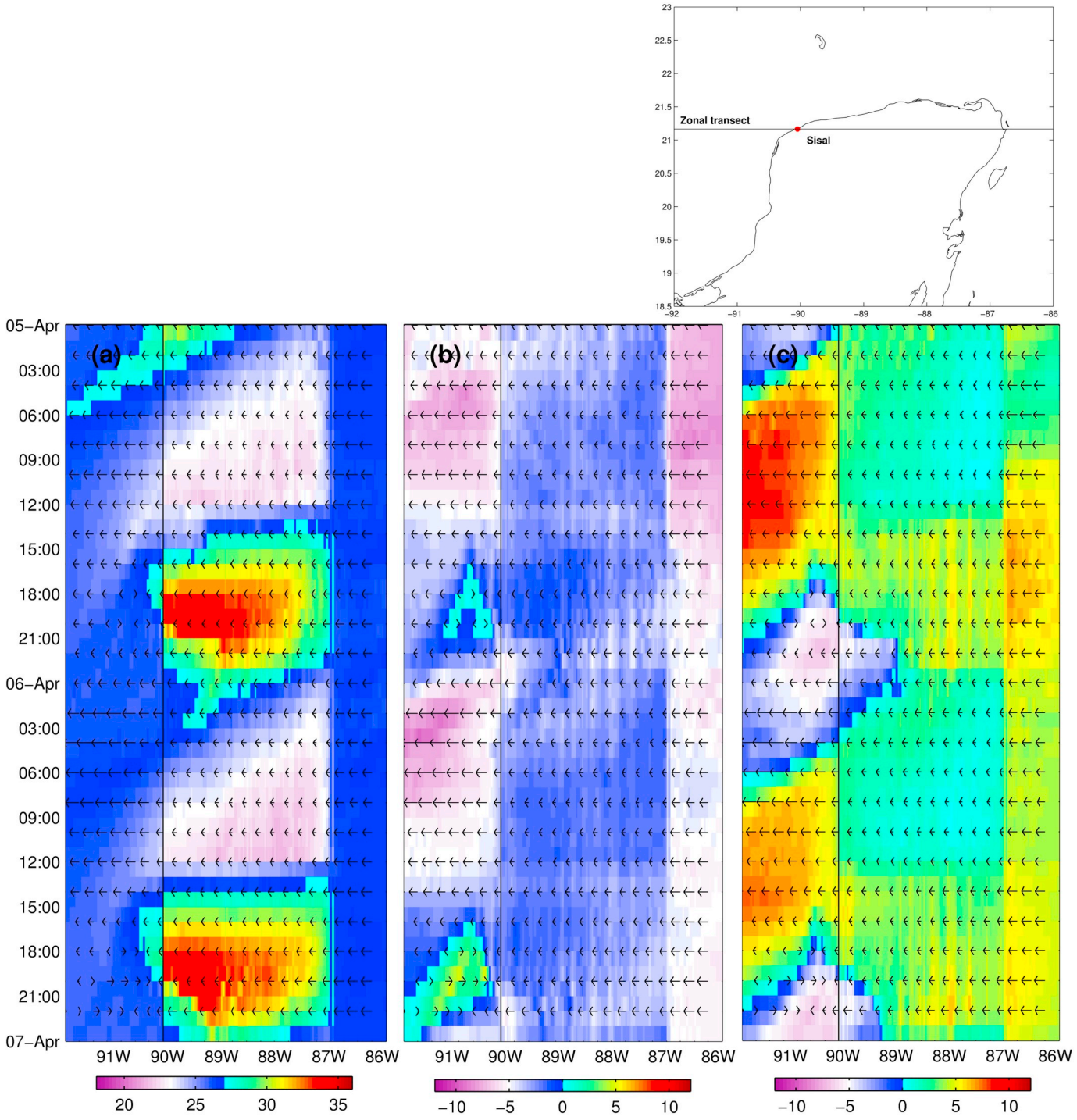

Fig. 9. Hovmöller diagram from d03 domain data, for a typical case of breeze. Zonal transect from April 5 at 00:00 h UTC to April 7 at 00:00 h UTC, which corresponds to April 4 at 18:00 h LT to April 6 at 18:00 h LT. The black line indicates the meridional position of Sisal (90° 02′ 26.44" W). (a) Air temperature at 2 m (°C), (b) zonal wind component u at 10 m (m s^{-1}), and (c) meridional wind component v at 10 m (m s^{-1}). The arrows represent the u component.

abrupt change in wind direction during the cold front passage through the YP region or a lag due to the horizontal wind displacement associated with thermal forcing (Haurwitz, 1947; Kusuda and Alpert, 1983; Alpert et al., 1984; Papanastasiou et al., 2010).

The land breeze is nullified while on the west coast there is a bending of the northerly wind due to the presence of the YP and easterly winds. The thermal difference that gives rise to the sea breeze during the cold front is minimum. With only a 4 °C temperature difference between the sea (20 °C) and land (24 °C), the sea breeze is restored at 00:00 h UTC (18:00 h LT) on April 11. These values are similar to those reported by Kishtawal et al. (2016) for the Bay of Bengal, India, and Miller et al. (2003). Nevertheless, the prevailing northerly wind minimizes the diurnal signal. The intrusion of the cold front reduces the mean easterly wind effect and the breeze front is not observed. On average breeze conditions, the YP cooling takes about 12 h (00:00 h to 12:00 h UTC, 18:00 h to 06:00 h LT), while during the CS event, it takes 6 h (00:00 h to 06:00 h UTC, 18:00 h to 00:00 h LT). The thermal difference decreases and hence it is associated with a greater stratification in the typical case of the breeze or with increased mixing in the atmospheric column in the case of the cold front (Stephan et al., 1999;

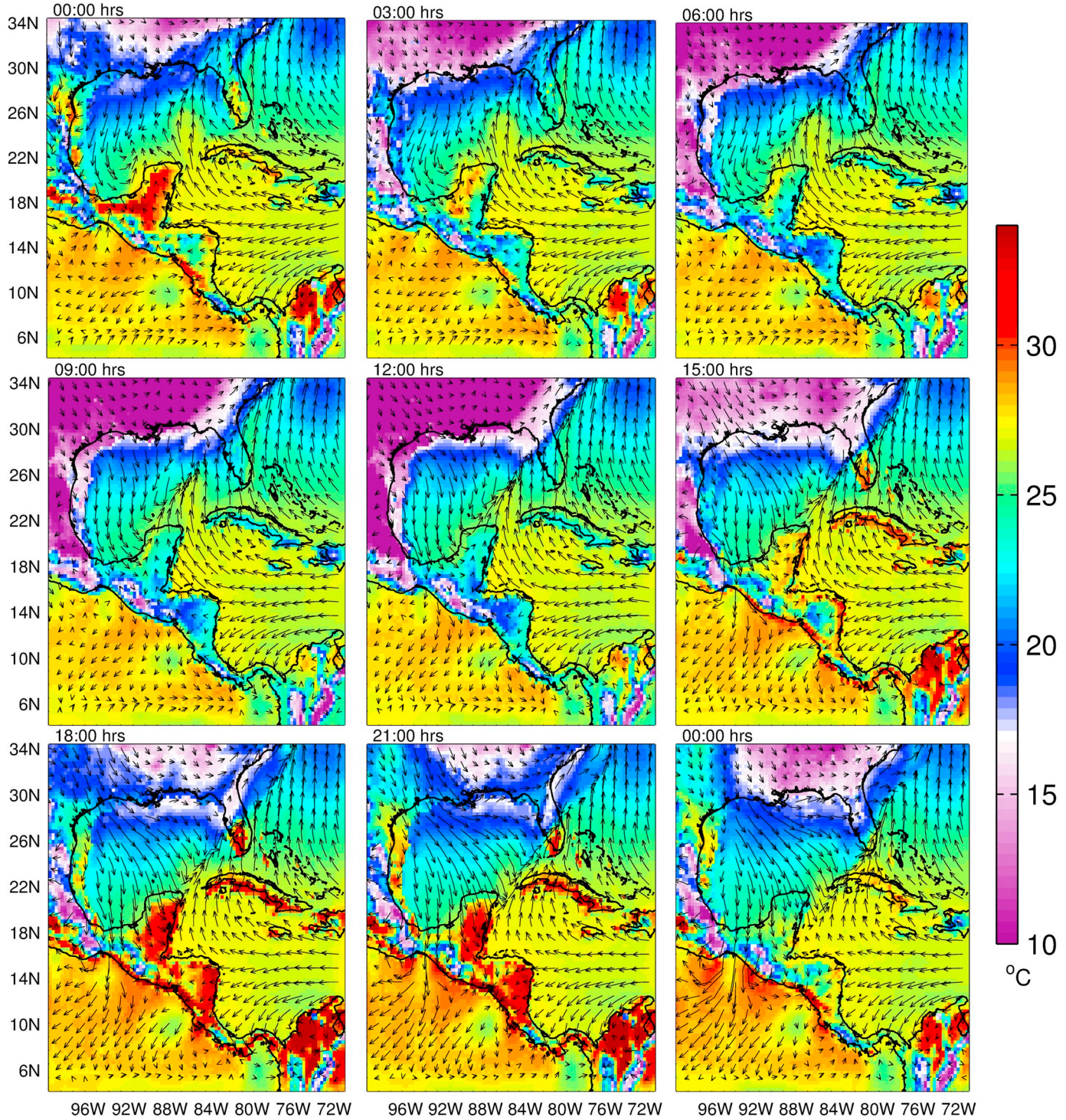

Fig. 10. Wind vectors at 10 m (ms^{-1}) and air temperature at 2 m (°C) (colored contours) for the CS event on April 8th in d01 domain. Maps are shown every three hrs from April 8 at 00:00 h UTC to April 9 at 00:00 h UTC, which corresponds to April 7 at 18:00 h LT to April 8 at 18:00 h LT.

Miller et al., 2003; Hu and Xue, 2015).

For this particular CS event, the front comes from the north-northwest, impacting the central and eastern zone of the GoM, the Peninsula of Florida, and the Caribbean Sea to Central America. A thermal front was generated between the continent and ocean northwest of the GoM, on the coasts of Louisiana and Texas, at 03:00 h UTC of April 8 (April 7 at 00:00 h LT) (Fig. 10). Three hours later, the cold front caused a significant decrease in wind intensity and a change of wind direction towards the northeast, from the YP through the Peninsula of Florida (Fig. 10). The arrival of the CS to the study area displaces the jet formed by the easterly winds to the south, below 18° N, giving rise to a convergence zone (Fig. 11). The average wind speed at Sisal during the CS event was 8 ms^{-1} with values up to 15 ms^{-1} in the GoM.

The development of the wind perpendicular to the coast (meridional component) is presented by the HM diagram shown in Fig. 12. Fig. 12a shows that sea-land diurnal thermal difference prevails, however, the tendency is towards maximum temperature decrease regarding to the average maximum temperature in a diurnal cycle, under breeze conditions. During the CS, average maximum temperature for the sea was less than 25 °C and less than 30 °C for land. The cold front penetrates

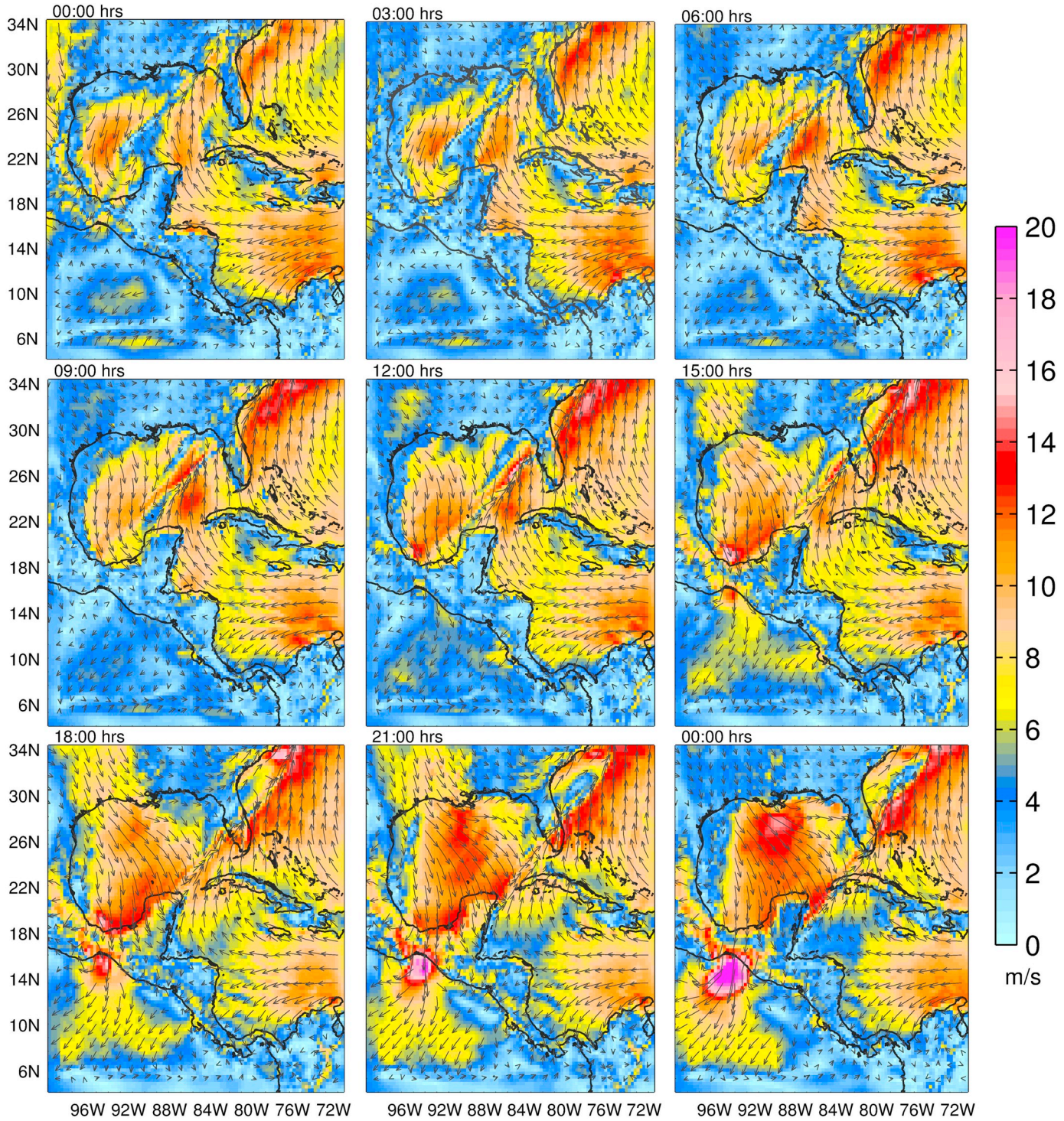

Fig. 11. Wind vectors and wind magnitude (colored contours) at 10 m (ms^{-1}) for the CS event on April 8th in d01 domain. Maps are shown every three hrs from April 8 at 00:00 h UTC to April 9 at 00:00 h UTC, which corresponds from April 7 at 18:00 h LT to April 8 at 18:00 h LT.

further inland and the presence of the mean easterly wind weakens (Fig. 12b). The impact of the cold front on local dynamics lasted 66 h, from April 8 at 12:00 h UTC (06:00 h LT) to April 11 at 06:00 h UTC (00:00 h LT). The diurnal cycle of the breeze was restored approximately in 3 h (April 11 from 06:00–09:00 h UTC, 00:00–03:00 h LT) after the CS left Sisal (Fig. 12c). However, differential heating over the YP occurs hours before the wind shifts and the diurnal cycle recovers, so that the zonal component becomes a key element for breeze recovery (Estoque, 1962; Gahmberg et al., 2010). On the other hand, the breeze front is not well defined under the CS conditions, however its arrival increases the magnitude of the winds in the YP and the Campeche Bank. It should be noted that although the signal of the breeze is preserved, the maximum intensity of the northerly wind is less than the maximum intensity of the diurnal signal.

When the meridional component of the mean wind direction changes drastically, the diurnal component is negatively affected and the diurnal signal relatively inhibited. The findings presented by Arritt (1993) and Gahmberg et al. (2010), determined that the extension and magnitude of the wind during a breeze event are directly related to the mesoscale dynamics. As in this study case the constant easterly wind

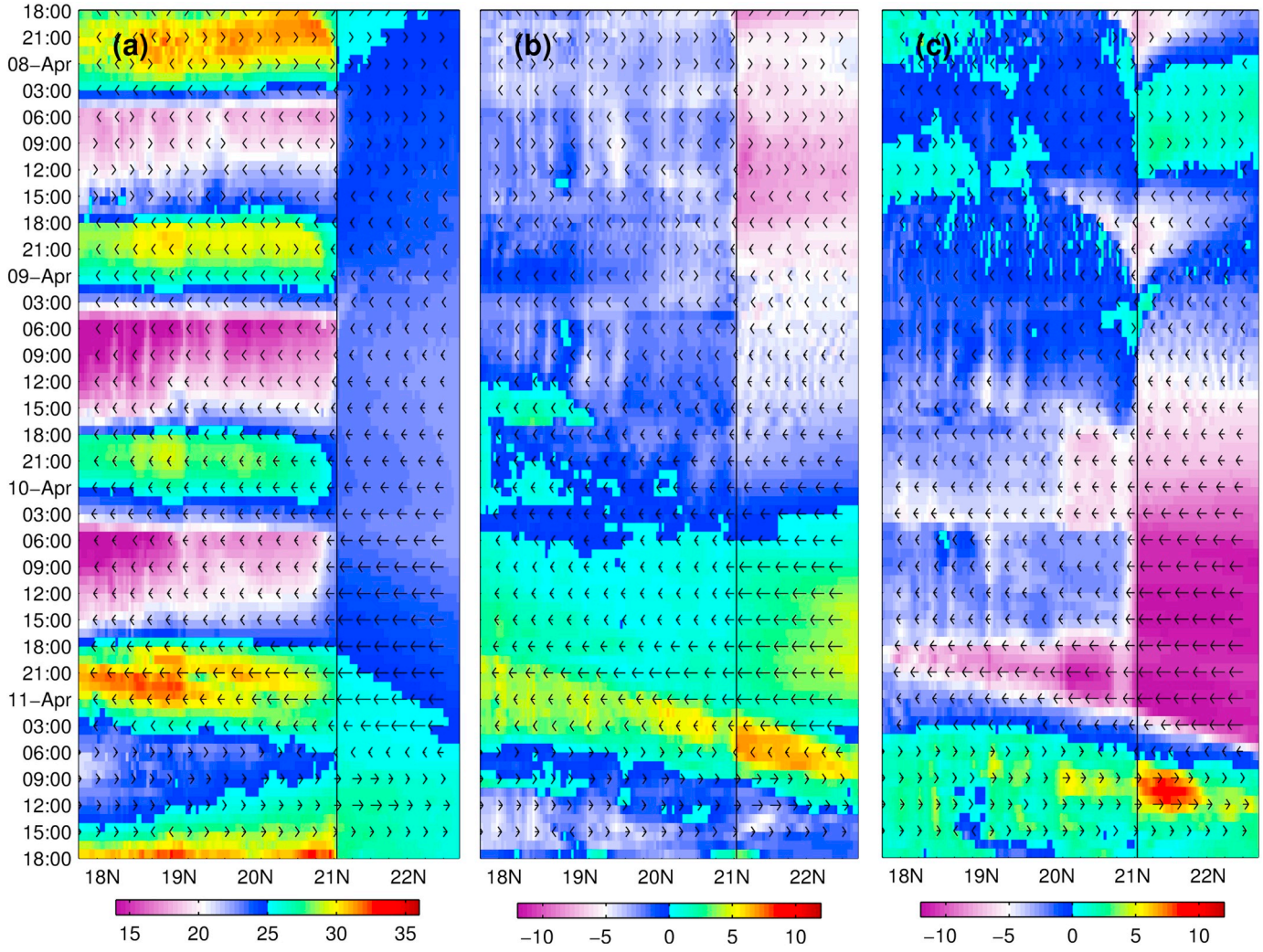

Fig. 12. Hovmöller diagram from d03 domain data, for the CS event. Meridional transect from April 7 at 18:00 h UTC to April 11 at 18:00 h UTC, which corresponds to April 7 at 12:00 h LT to April 11 at 12:00 h LT. The black line indicates the latitudinal position of Sisal (21° 09′ 56.20" N). (a) Air temperature at 2 m (°C), (b) zonal wind component u at 10 m ($m\,s^{-1}$), and (c) meridional wind component v at 10 m ($m\,s^{-1}$). The arrows represent the v component.

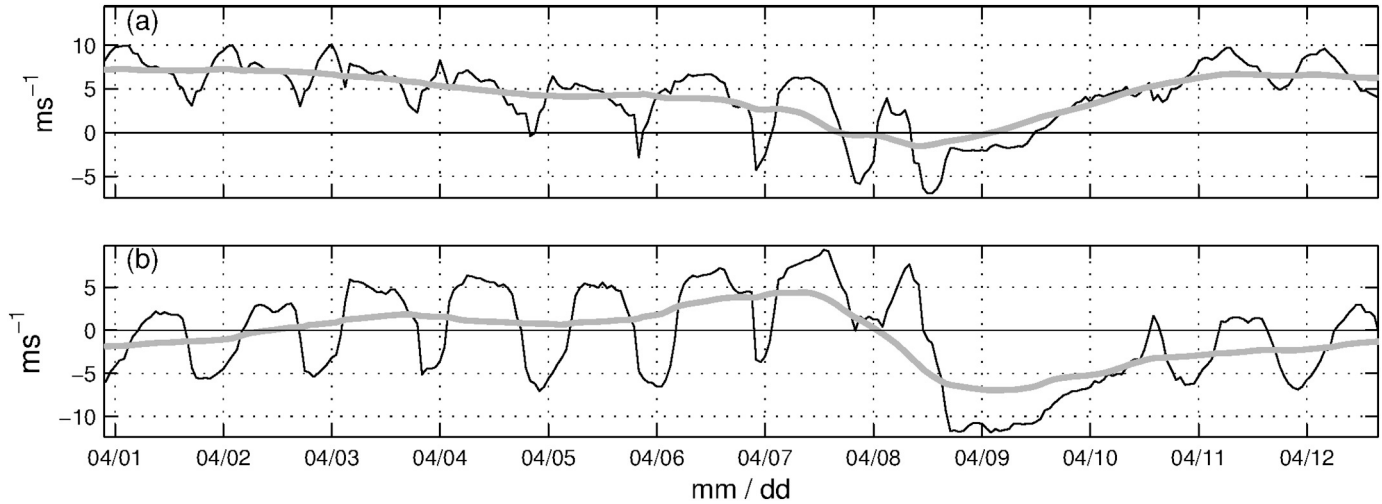

Fig. 13. Time series of wind speed components at 10 m (ms^{-1}) from WRF-d03 in Sisal, Yuc. (21° 09′ 56.20" N, 90° 02′ 26.44" W). (a) Zonal and (b) meridional component. The black line represents the hourly wind speed, and the gray line represents the low-pass filtered wind speed with a 24-h cut-off frequency.

(Fig. 13a), also promotes an atmospheric dynamics perpendicular to the coastline (Fig. 13b) which aligns with the sea-land temperature gradient (Azorin-Molina et al., 2011; Hughes and Veron, 2018). The above is shown by the high eccentricity values obtained, added to the effect of latitude (Alpert et al., 1984) due to the study area location. The geographical variability of the signal modulates not only its eccentricity, but also its amplitude. The Coriolis effect does not influence this wind perpendicular alignment to the coastline and its large spatial extent. Below 30°, the Coriolis force (f) is relatively small and its frequency is less than the inertial frequency (ω) (Rotunno, 1983), in this study case the diurnal frequency (24 h), which allows the breeze front to propagate before being deflected by the Coriolis effect. Hence, when $f < \omega$ the breeze occurs as inertial internal waves or gravity waves, which increase the extension of the breeze (Garratt et al., 1988; Buckley and Kurzeja, 1997; van der Wiel et al., 2017). Nevertheless, the Coriolis effect is significant for the development of the diurnal signal, since otherwise there would be a decrease in the eccentricity and tilt with respect to the coastline during the trajectory of the wind. Also, the influence of this effect is evident in the direction of the ellipses' rotation (Kusuda and Alpert, 1983; Alpert et al., 1984; Simpson, 1996), and is also modulated by the interaction between the mean wind and the forces associated with the horizontal pressure gradients (Leopold, 1949; Martin and Pielke, 1983; Neumann, 1977, 1984; Atkins and Wakimoto, 1997).

5. Conclusions

We analyzed the breeze dynamics and its interaction with a cold surge event in the Yucatan Peninsula utilizing a high-resolution numerical model. Study of the interaction between meteorological systems is of great importance because both dynamic and thermodynamic processes are frequently modified, as in the case of the breeze phenomenon. The WRF model was successfully validated with observed data from meteorological stations located in the YP region and an ultrasonic sensor located in Sisal on the YP coast, which were collected during spring 2014. The numerical model allowed us to investigate the conditions of the local atmosphere at different temporal scales, as well as its spatial variability and the influence of mesoscale atmospheric phenomena characteristic of the study area (i.e., CS events). The magnitude of the wind diurnal component found in this study, is greater than that computed by Gille et al. (2005) for the entire planet, by exceeding 10 ms^{-1}. Some of the main factors that controlled the mechanisms of the breezes in Sisal during the study period, were:

(i) The sea-land thermal gradient shows a strong asymmetry between the land and sea breezes, where the intensity of the diurnal signal increases as the thermal difference reaches its maximum. Moreover, the easterly winds favor the surface cooling during the night, intensifying the thermal gradient as well as the land breeze.

(ii) The geographic location of the YP favors the diurnal signal amplitude since at this latitude, the frequency of the signal is lower than the inertial frequency.

(iii) The synoptic wind and the mesoscale atmospheric stability also modulates the breeze dynamics, with a reduction in the diurnal signal amplitude in response to the arrival of a CS or when the easterly winds intensify.

(iv) The coastline orientation favors the deflection of the winds along the northwest coast caused by the appearance of the sea breeze, which, in turn, generates a more intense southern wind component.

(v) Breeze dynamics are also influenced by the effect of surface friction, the low altitude above sea level, and the interactions between the previous factors (i-iv).

In general, during a diurnal cycle, the meridional component intensification determines the sea breeze landwards penetration while the wind convergence zone intensifies the effect of the land breeze, which penetrates further offshore. This land breeze intensification makes the diurnal signal exceeds the local spatial scale, even though breezes are originated by differential heating at a local scale. This synoptic-scale phenomena of the breeze observed in the YP region can be considered as symmetrical in terms of their components, which suggest a north-south atmospheric dynamics or vice versa, even with the arrival of a moderate CS event. The current results cannot be generalized for other CS events with different characteristics of intensity and displacement. Hence, further research on breeze-CS interaction is warranted.

Acknowledgements

Financial support was provided by the National Council of Science and Technology (CONACyT) through Cátedras-CONACyT program (Coastal Observatory for studies of resilience to climate change-1146), the National Coastal Resilience Laboratory (LN-293354), and the SENER-CONACyT-201441. The first author acknowledges the financial support from the Engineering Institute at UNAM through the internal project Observatorio Costero. Thanks to the National Meteorological Service, to the Secretaría de Marina, and to the Comisión Federal de Electricidad through the project of Boundary-Layer for providing the meteorological stations database of the YP region. Thanks to the European Center for Medium-Range Weather Forecasts for providing the ERA-Interim database and the National Center for Atmospheric Research sponsored by the National Science Foundation for making the WRF development. We acknowledge Gonzalo Uriel Martin Ruiz for IT technical support.

Declaration of Competing Interests

None.

References

Alpert, P., Kusuda, M., Abe, N., 1984. Anticlockwise Rotation, Eccentricity and Tilt Angle of the Wind Hodograph. Part II: An Observational Study. J. Atmos. Sci. 41, 3568–3583. https://doi.org/10.1175/1520-0469(1984)041<3568:areata>2.0.co;2.

Appendini, C.M., Torres-Freyermuth, A., Salles, P., López-González, J., Mendoza, E.T., 2014. Wave climate and trends for the Gulf of Mexico: a 30-yr wave hindcast. J. Clim. 27, 1619–1632. https://doi.org/10.1175/JCLI-D-13-00206.1.

Appendini, C.M., Hernández-Lasheras, J., Meza-Padilla, R., Kurczyn, J.A., 2018. Effect of climate change on wind waves generated by anticyclonic cold front intrusions in the Gulf of Mexico. Clim. Dyn. 51, 3747–3763. https://doi.org/10.1007/s00382-018-4108-4.

Arritt, R.W., 1993. Effects of the Large-Scale Flow on Characteristic Features of the Sea Breeze. J. Appl. Meteorol. 32, 116–125. https://doi.org/10.1175/1520-0450(1993)032<0116:eotlsf>2.0.

Asimakopoulos, D.N., Helmis, C.G., Papadopoulos, K.H., Kalogiros, J.A., Kassomenos, P., Petrakis, M., 1999. Inland propagation of sea breeze under opposing offshore wind. Meteorog. Atmos. Phys. 70, 97–110. https://doi.org/10.1007/s007030050027.

Asuero, A.G., Sayago, A., González, A.G., 2006. The Correlation Coefficient: an Overview. Crit. Rev. Anal. Chem. 36, 41–59.

Atkins, N.T., Wakimoto, R.M., 1997. Influence of the Synoptic-Scale Flow on Sea Breezes Observed during CaPE. Mon. Weather Rev. 125, 2112–2130. https://doi.org/10.1175/1520-0493(1997)125<2112:iotssf>2.0.co;2.

Atkins, N.T., Wakimoto, R.M., Weckwerth, T.M., 1995. Observations of the Sea-Breeze Front during CaPE. Part II: Dual-Doppler and Aircraft Analysis. Mon. Weather Rev. 123, 944–969. https://doi.org/10.1175/1520-0493(1995)123<0944:ootsbf>2.0.co;2.

Atkinson, B.W., Zhang, J.W., 1996. Mesoscale shallow convection in the atmosphere. Rev. Geophys. 34, 403–431. https://doi.org/10.1029/96RG02623.

Azorin-Molina, C., Chen, D., Tijm, S., Baldi, M., 2011. A multi-year study of sea breezes in a Mediterranean coastal site: Alicante (Spain). Int. J. Climatol. 31, 468–486. https://doi.org/10.1002/joc.2064.

Beljaars, A.C.M., 1995. The parametrization of surface fluxes in large-scale models under free convection. Q. J. R. Meteorol. Soc. 121, 255–270. https://doi.org/10.1002/qj.49712152203.

Birch, C.E., Roberts, M.J., Garcia-Carreras, L., Ackerley, D., Reeder, M.J., Lock, A.P., Schiemann, R., 2015. Sea-breeze dynamics and convection initiation: the influence of convective parameterization in weather and climate model biases. J. Clim. 28, 8093–8108. https://doi.org/10.1175/JCLI-D-14-00850.1.

Bolgiani, P., Fernández-Gonzáez, S., Valero, S., Merino, A., García-Ortega, E., Sánchez, J.L., Martín, M.L., 2018. Numerical simulation of a Heavy Precipitation Event in the Vicinity of Madrid-Barajas International Airport: Sensitivity to initial Conditions, Domain Resolution, and Microphysics Parameterizations. Atmosphere. 9, 329.

Buckley, R.L., Kurzeja, R.J., 1997. An Observational and Numerical Study of the Nocturnal Sea Breeze. Part I: Structure and Circulation. J. Appl. Meteorol. 36, 1577–1598. https://doi.org/10.1175/1520-0450(1997)036<1577:aoanso>2.0.

co;2.
Carvalho, D., Rocha, A., Gómez-Gesteira, M., Santos, C., 2012. A sensitivity study of the WRF model in wind simulation for an area of high wind energy. Environ. Model. Softw. 33, 23–34. https://doi.org/10.1016/j.envsoft.2012.01.019.
Carvalho, D., Rocha, A., Gómez-Gesteira, M., Silva Santos, C., 2014. WRF wind simulation and wind energy production estimates forced by different reanalyses: Comparison with observed data for Portugal. Appl. Energy 117, 116–126. https://doi.org/10.1016/j.apenergy.2013.12.001.
Chai, T., Draxler, R.R., 2014. Root mean square error (RMSE) or mean absolute error (MAE)? – Arguments against avoiding RMSE in the literature. Geosci. Model Dev. 7, 1247–1250. https://doi.org/10.5194/gmd-7-1247-2014.
Challa, V.S., Indracanti, J., Rabarison, M.K., Patrick, C., Baham, J.M., Young, J., Hughes, R., Hardy, M.G., Swanier, S.J., Yerramilli, A., 2009. A simulation study of mesoscale coastal circulations in Mississippi Gulf coast. Atmos. Res. 91, 9–25. https://doi.org/10.1016/j.atmosres.2008.05.004.
Davis, J., 2003. Statistics and data analysis in geology. Technometrics. https://doi.org/10.1080/00401706.1987.10488290.
Davis, R.E., O'Donnell, J., Ackleson, S.G., Rowe, C.M., Feddema, J.J., Willmott, C.J., Legates, D.R., Klink, K.M., 1985. Statistics for the evaluation and comparison of models. J. Geophys. Res. 90, 8995. https://doi.org/10.1029/jc090ic05p08995.
Day, B.M., Rappenglück, B., Clements, C.B., Tucker, S.C., Alan Brewer, W., 2010. Nocturnal boundary layer characteristics and land breeze development in Houston, Texas during TexAQS II. Atmos. Environ. 44, 4014–4023. https://doi.org/10.1016/j.atmosenv.2009.01.031.
DiMego, G.J., Bosart, L.F., Endersen, G.W., 1976. An Examination of the Frequency and mean Conditions Surrounding Frontal Incursions into the Gulf of Mexico and Caribbean Sea. Mon. Weather Rev. 104, 709–718. https://doi.org/10.1175/1520-0493(1976)104<0709:aeotfa>2.0.co;2.
Dudhia, J., 1989. Numerical Study of Convection Observed during the Winter Monsoon Experiment using a Mesoscale Two-Dimensional Model. J. Atmos. Sci. 46, 3077–3107. https://doi.org/10.1175/1520-0469(1989)046<3077:nsocod>2.0.co;2.
Dyer, A.J., Hicks, B.B., 1970. Flux-gradient relationships in the constant flux layer. Q. J. R. Meteorol. Soc. 96, 715–721. https://doi.org/10.1002/qj.49709641012.
ECMWF, 2006. ERA-Interim [WWW Document]. Atmos. Data, URL. http://apps.ecmwf.int/datasets/data/interim-full-daily/levtype=sfc/.
Enriquez, C., Mariño-Tapia, I.J., Herrera-Silveira, J.A., 2010. Dispersion in the Yucatan coastal zone: Implications for red tide events. Cont. Shelf Res. 30, 127–137. https://doi.org/10.1016/j.csr.2009.10.005.
Estoque, M.A., 1962. The Sea Breeze as a Function of the Prevailing Synoptic Situation. J. Atmos. Sci. 19, 244–250. https://doi.org/10.1175/1520-0469(1962)019<0244:tsbaaf>2.0.co;2.
Fernández-González, S., Martín, M.L., Merino, A., Sánchez, J.L., Valero, F., 2017. Uncertainty quantification and predictability of wind speed over the Iberian Peninsula. J. Geophys. Res. 122, 3877–3890. https://doi.org/10.1002/2017JD026533.
Fernández-González, S., Martín, M.L., García-Ortega, E., Merino, A., Lorenzana, J., Sánchez, J.L., Valero, F., Rodrigo, J.S., 2018. Sensitivity analysis of the WRF model: Wind-resource assessment for complex terrain. J. Appl. Meteorol. Climatol. 75, 733–753. https://doi.org/10.1175/JAMC-D-17-0121.1.
Figueroa-Espinoza, B., Salles, P., Zavala-Hidalgo, J., 2014. On the wind power potential in the northwest of the Yucatan Peninsula in Mexico. Atmosfera 27, 77–89. https://doi.org/10.1016/S0187-6236(14)71102-6.
Fisher, N.I., 1995. Statistical Analysis of Circular Data. Cambridge University Press, Cambridge 277 pp.
Fisher, N.I., Lee, A.J., 1983. A correlation coefficient for circular data. Biometrika 70, 327–332. https://doi.org/10.1093/biomet/70.2.327.
Fita, L., Gutiérrez, J.M., Fernández, J., Méndez, F.J., García-Díez, M., Menendez, M., 2013. High-resolution Sea wind hindcasts over the Mediterranean area. Clim. Dyn. 42, 1857–1872. https://doi.org/10.1007/s00382-013-1912-8.
Fonseca, R., Koh, T.Y., Teo, C.K., 2019. Multi-scale interactions in a high-resolution tropical-belt experiment and observations. Clim. Dyn. 52, 3503. https://doi.org/10.1007/s00382-018-4332-y.
Gahmberg, M., SavijäRVI, H., Leskinen, M., 2010. The influence of synoptic scale flow on sea breeze induced surface winds and calm zones. Tellus, Ser. A Dyn. Meteorol. Oceanogr. 62, 209–217. https://doi.org/10.1111/j.1600-0870.2009.00423.x.
Garratt, J.R., Howells, P.A.C., Kowalczyk, E., 1988. The Behavior of Dry Cold Fronts traveling along a Coastline. Mon. Weather Rev. 117, 1208–1220. https://doi.org/10.1175/1520-0493(1989)117<1208:tbodcf>2.0.co;2.
Gentry, R.C., Moore, P.L., 1954. Relation of local and General Wind Interaction near the Sea Coast to Time and Location of Air-Mass Showers. J. Meteorol. 11, 507–511. https://doi.org/10.1175/1520-0469(1954)011<0507:rolagw>2.0.co;2.
Giffen, D., Raubenheimer, B., Signell, R.P., Elgar, S., Ralston, D.K., 2012. Observations and predictions of summertime winds on the Skagit tidal flats. Washington. Cont. Shelf Res. 60, S13–S21. https://doi.org/10.1016/j.csr.2012.02.001.
Gille, S.T., Llewellyn Smith, S.G., Lee, S.M., 2003. Measuring the sea breeze from QuikSCAT Scatterometry. Geophys. Res. Lett. 30. https://doi.org/10.1029/2002GL016230.
Gille, S.T., Llewellyn Smith, S.G., Statom, N.M., 2005. Global observations of the land breeze. Geophys. Res. Lett. 32, 1–4. https://doi.org/10.1029/2004GL022139.
Givati, A., Lynn, B., Liu, Y., Rimmer, A., 2012. Using the WRF model in an Operational Streamflow Forecast System for the Jordan River. J. Appl. Meteorol. Climatol. 51, 285–299. https://doi.org/10.1175/JAMC-D-11-082.1.
Golub, G.H., Reinsch, C., 1971. Singular Value Decomposition and Least Squares Solutions. In: Bauer, F.L. (Ed.), Linear Algebra. Handbook for Automatic Computation. 2 Springer, Berlin, Heidelberg.
Goodwin, P., Lawton, R., 1999. On the asymmetry of the symmetric MAPE. Int. J. Forecast. 15, 405–408. https://doi.org/10.1016/S0169-2070(99)00007-2.
Gunwani, P., Mohan, M., 2017. Sensitivity of WRF model estimates to various PBL parameterizations in different climatic zones over India. Atmos. Res. 194, 43–65.
Harmel, R.D., Veith, T.L., Arnold, J.G., Van Liew, M.W., Bingner, R.L., Moriasi, D.N., 2007. Model Evaluation guidelines for Systematic Quantification of Accuracy in Watershed Simulations. Trans. ASABE 50, 885–900. https://doi.org/10.13031/2013.23153.
Haurwitz, B., 1947. Comments on the Sea-Breeze Circulation. J. Meteorol. 4, 1–8. https://doi.org/10.1175/1520-0469(1947)004<0001:cotsbc>2.0.co;2.
Hendrickson, J., MacMahan, J., 2009. Diurnal Sea breeze effects on inner-shelf cross-shore exchange. Cont. Shelf Res. 29, 2195–2206. https://doi.org/10.1016/j.csr.2009.08.011.
Hong, S.-Y., Dudhia, J., Chen, S.-H., 2004. A revised Approach to Ice Microphysical Processes for the Bulk Parameterization of Clouds and Precipitation. Mon. Weather Rev. 132, 103–120. https://doi.org/10.1175/1520-0493(2004)132<0103:aratim>2.0.co;2.
Hong, S.-Y., Noh, Y., Dudhia, J., 2006. A New Vertical Diffusion Package with an Explicit Treatment of Entrainment Processes. Mon. Weather Rev. 134, 2318–2341. https://doi.org/10.1175/mwr3199.1.
Hsu, S.A., 2013. Coastal Meteorology, Coastal Meteorology. https://doi.org/10.1016/C2009-0-21713-2.
Hu, X.-M., Xue, M., 2015. Influence of Synoptic Sea-Breeze Fronts on the Urban Heat Island Intensity in Dallas–Fort Worth. Texas. Mon. Weather Rev. 144, 1487–1507. https://doi.org/10.1175/mwr-d-15-0201.1.
Hughes, C.P., Veron, D.E., 2018. A characterization of the Delaware Sea breeze using observations and modeling. J. Appl. Meteorol. Climatol. 57, 1405–1421. https://doi.org/10.1175/JAMC-D-17-0186.1.
Jammalamadaka, S.R., Sarma, Y., 1988. A correlation coefficient for angular variables. In: Statistical Thoery and Data Analysis II. Tokyo, pp. 349–364.
Kain, J.S., 2004. The Kain-Fritsch convective parameterization: an update. J. Appl. Meteorol. 43, 170–181. https://doi.org/10.1175/1520-0450(2004)043<0170:TKCPAU>2.0.CO;2.
Kingsmill, D.E., 1995. Convection Initiation Associated with a Sea-Breeze Front, a Gust Front, and their Collision. Mon. Weather Rev. 123, 2913–2933. https://doi.org/10.1175/1520-0493(1995)123<2913:ciawas>2.0.co;2.
Kishtawal, C.M., Rajasekhar, M., Sathiyamoorthy, V., Kesarkar, A.P., Bhate, J., Karipot, A., Bala Subrahamanyam, D., 2016. A sea breeze induced thunderstorm over an in-land station over Indian south Peninsula – a case study. J. Atmos. Solar-Terrestrial Phys. 148, 96–111. https://doi.org/10.1016/j.jastp.2016.09.002.
Kozo, T.L., 1982. An Observational Study of Sea Breezes along the Alaskan Beaufort Sea Coast: part I. J. Appl. Meteorol. 21, 891–905. https://doi.org/10.1175/1520-0450(1982)021<0891:aososb>2.0.co;2.
Kusuda, M., Alpert, P., 1983. Anti-Clockwise Rotation of the Wind Hodograph. Part I: Theoretical Study. J. Atmos. Sci. 40, 487–499. https://doi.org/10.1175/1520-0469(1983)040<0487:acrotw>2.0.co;2.
Lawson, C., Hanson, R., 1974. Solving Least Square Problems. Prentice Hall 340 pp.
Legates, D.R., Mccabe, G.J., 2013. A refined index of model performance: a rejoinder. Int. J. Climatol. 33, 1053–1056. https://doi.org/10.1002/joc.3487.
Leopold, L.B., 1949. The Interaction of Trade Wind and Sea Breeze. Hawaii. J. Meteorol. 6, 312–320. https://doi.org/10.1175/1520-0469(1949)006<0312:tiotwa>2.0.co;2.
Li, Y.K., Chao, J.P., 2016. An analytical solution for three-dimensional sea-land breeze. J. Atmos. Sci. 73. https://doi.org/10.1175/JAS-D-14-0329.1.
LIPC UNAM, 2017. Observatorio costero del sureste [WWW Document]. Wind data. URL. http://ocse.mx/en/experimento/torre-sisal.
Manobianco, J., Case, J.L., Roeder, W.P., Wheeler, M.M., Weems, J.W., 2005. A 7-Yr Climatological Study of Land Breezes over the Florida Spaceport. J. Appl. Meteorol. 44, 340–356. https://doi.org/10.1175/jam-2202.1.
Mardia, K.V., Jupp, P.E., 2008. Directional Statistics. John Wiley and Sons Ltd.https://doi.org/10.1002/9780470316979. 432 pp.
Martin, C.L., Pielke, R.A., 1983. The Adequacy of the Hydrostatic Assumption in Sea Breeze Modeling over Flat Terrain. J. Atmos. Sci. 40, 1472–1481. https://doi.org/10.1175/1520-0469(1983)040<1472:taotha>2.0.co;2.
Masselink, G., Pattiaratchi, C., 1998a. The effect of sea breeze on beach morphology, surf zone hydrodynamics and sediment resuspension. Mar. Geol. 146, 115–135. https://doi.org/10.1016/S0025-3227(97)00121-7.
Masselink, G., Pattiaratchi, C., 1998b. Morphodynamic impact of sea breeze activity on a beach with beach cusp morphology. J. Coast. Res. 14, 393–406.
Medellín, G., Torres-Freyermuth, A., Tomasicchio, G.R., Francone, A., Tereszkiewicz, P.A., Lusito, L., Palemón-Arcos, L., López, J., 2018. Field and numerical study of resistance and resilience on a sea breeze dominated beach in Yucatan (Mexico). Water (Switzerland) 10. https://doi.org/10.3390/w10121806.
Miller, S.T.K., Keim, B.D., Talbot, R.W., Mao, H., 2003. Sea breeze: Structure, forecasting, and impacts. Rev. Geophys. 41. https://doi.org/10.1029/2003RG000124.
Molinari, J., Knight, D., Dickinson, M., Vollaro, D., Skubis, S., 1997. Potential Vorticity, Easterly Waves, and Eastern Pacific Tropical Cyclogenesis. Mon. Weather Rev. 125 (10), 2699–2708.
Neumann, J., 1977. On the Rotation Rate of the direction of Sea and Land Breezes. J. Atmos. Sci. 34, 1913–1917.
Neumann, J., 1984. The Coriolis Force in Relation to the Sea and Land Breezes—a Historical note. Bull. Am. Meteorol. Soc. 65, 24–26. https://doi.org/10.1175/1520-0477(1984)065<0024:tcfirt>2.0.co;2.
Novitsky, M., Reible, D.D., Corripio, B.M., 1992. Modeling the dynamics of the land-sea breeze circulation for air quality modeling. Boundary-Layer Meteorol. 59, 163–175. https://doi.org/10.1007/BF00120692.
Papanastasiou, D.K., Melas, D., Lissaridis, I., 2010. Study of wind field under sea breeze

conditions; an application of WRF model. Atmos. Res. 98, 102–117. https://doi.org/10.1016/j.atmosres.2010.06.005.
Paulson, C.A., 1970. The Mathematical Representation of Wind speed and Temperature Profiles in the Unstable Atmospheric Surface Layer. J. Appl. Meteorol. 9, 857–861. https://doi.org/10.1175/1520-0450(1970)009<0857:tmrows>2.0.co;2.
Ponce de León, S., Orfila, A., 2013. Numerical study of the marine breeze around Mallorca Island. Appl. Ocean Res. 40, 26–34. https://doi.org/10.1016/j.apor.2012.12.003.
Robinson, W.S., 1957. The Statistical Measurement of Agreement. Am. Sociol. Rev. 22, 17. https://doi.org/10.2307/2088760.
Rotunno, R., 1983. On the Linear Theory of the Land and Sea Breeze. J. Atmos. Sci. 40, 1999–2009. https://doi.org/10.1175/1520-0469(1983)040<1999:otltot>2.0.co;2.
Schmidt, F.H., 1947. An Elementary Theory of the Land- and Sea-Breeze Circulation. J. Meteorol. 4, 9–20. https://doi.org/10.1175/1520-0469(1947)004<0009:aetotl>2.0.co;2.
Schwartz, C.S., 2014. Reproducing the September 2013 Record-breaking Rainfall over the Colorado Front Range with High-Resolution WRF forecasts. Weather Forecast. 29, 393–402. https://doi.org/10.1175/waf-d-13-00136.1.
Senatore, A., Mendicino, G., Knoche, H.R., Kunstmann, H., 2014. Sensitivity of Modeled Precipitation to Sea Surface Temperature in Regions with complex Topography and Coastlines: a Case Study for the Mediterranean. J. Hydrometeorol. 15, 2370–2396.
Sepp, M., Jaagus, J., 2002. Frequency of circulation patterns and air temperature variations in Europe. Boreal Environ. Res. 7, 273–279.
Serra, Y.L., Kiladis, G.N., Hodges, K.I., 2010. Tracking and mean structure of easterly waves over the Intra-Americas Sea. J. Clim. 23 (18), 4823–4840.
Simpson, J.E., 1996. Diurnal changes in Sea-Breeze direction. J. Appl. Meteorol. 35, 1166–1169. https://doi.org/10.1175/1520-0450(1996)035<1166:dcisbd>2.0.co;2.
Skamarock, W.C., Klemp, J.B., Dudhia, J., Gill, D.O., Barker, D., Duda, M.G., Xiang-Yu, H., Wang, W., 2008. A Description of the Advanced Research WRF Version 3. https://doi.org/10.13140/RG.2.1.2310.6645.
Srinivas, C.V., Venkatesan, R., Somayaji, K.M., Bagavath Singh, A., 2006. A numerical study of sea breeze circulation observed at a tropical site Kalpakkam on the east coast of India, under different synoptic flow situations. J. Earth Syst. Sci. 115, 557–574. https://doi.org/10.1007/BF02702909.
Stephan, K., Kraus, H., Ewenz, C.M., Hacker, J.M., 1999. Sea-breeze front variations in space and time. Meteorog. Atmos. Phys. 70, 81–95. https://doi.org/10.1007/s007030050026.
Suresh, R., 2007. Observation of sea breeze front and its induced convection over Chennai in Southern Peninsular India using Doppler Weather Radar. In: Pure and Applied Geophysics, pp. 1511–1525. https://doi.org/10.1007/s00024-007-0234-3.
Taubman, S.J., Clough, S.A., Iacono, M.J., Brown, P.D., Mlawer, E.J., 1997. Radiative transfer for inhomogeneous atmospheres: RRTM, a validated correlated-k model for the longwave. J. Geophys. Res. Atmos. 102, 16663–16682. https://doi.org/10.1029/97jd00237.
Taylor-Espinosa, N.E., 2009. Análisis y visualización de la componente diurna de los vientos en el sur del Golfo de México. (UNAM).
Taylor-Espinosa, N.E., 2014. Estudio de la variabilidad diurna de los vientos en el sur del Golfo de México. (UNAM).
Tewari, M., Chen, F., Wang, W., Dudhia, J., LeMone, M.A., Mitchell, K., Ek, M., Gayno, G., Wegiel, J., Cuenca, R.H., 2004. Implementation and verification of the unified NOAH land surface model in the WRF model (formerly Paper Number 17.5). In: 20th Conference on Weather Analysis and Forecasting/16th Conference on Numerical Weather Prediction. Pp, pp. 11–15.
Torres-Freyermuth, A., Puleo, J.A., DiCosmo, N., Allende-Arandía, M.E., Chardón-Maldonado, P., López, J., Figueroa-Espinoza, B., de Alegria-Arzaburu, A.R., Figlus, J., Roberts Briggs, T.M., de la Roza, J., Candela, J., 2017. Nearshore circulation on a sea breeze dominated beach during intense wind events. Cont. Shelf Res. 151. https://doi.org/10.1016/j.csr.2017.10.008.
Uppala, S.M., Healy, S.B., Balmaseda, M.A., de Rosnay, P., Isaksen, L., van de Berg, L., Geer, A.J., McNally, A.P., Matricardi, M., Haimberger, L., Dee, D.P., Dragani, R., Bormann, N., Hersbach, H., Vitart, F., Kobayashi, S., Andrae, U., Beljaars, A.C.M., Poli, P., Monge-Sanz, B.M., Peubey, C., Thépaut, J.-N., Delsol, C., Hólm, E.V., Simmons, A.J., Köhler, M., Bechtold, P., Berrisford, P., Balsamo, G., Park, B.-K., Fuentes, M., Bidlot, J., Bauer, P., Tavolato, C., Kållberg, P., Morcrette, J.-J., 2011. The ERA-Interim reanalysis: configuration and performance of the data assimilation system [WWW Document]. Q. J. R. Meteorol. Soc. https://doi.org/10.1002/qj.828 (accessed December 2016).
Van Delden, A., 2000. The synoptic setting of thunderstorms in Western Europe. Atmos. Res. 56, 89–110. https://doi.org/10.1016/S0169-8095(00)00092-2.
Wakimoto, R.M., Atkins, N.T., 1994. Observations of the Sea-Breeze Front during CaPE. Part I: Single-Doppler, Satellite, and Cloud Photogrammetry Analysis. Mon. Weather Rev. 122, 1092–1114. https://doi.org/10.1175/1520-0493(1994)122<1092:ootsbf>2.0.co;2.
Webb, E.K., 1970. Profile relationships: the log-linear range, and extension to strong stability. Q. J. R. Meteorol. Soc. 96, 67–90. https://doi.org/10.1002/qj.49709640708.
van der Wiel, K., Gille, S.T., Llewellyn Smith, S.G., Linden, P.F., Cenedese, C., 2017. Characteristics of colliding sea breeze gravity current fronts: a laboratory study. Q. J. R. Meteorol. Soc. 143, 1434–1441. https://doi.org/10.1002/qj.3015.
Willmott, C.J., 1982. Some comments on the Evaluation of Model Performance. Bull. Am. Meteorol. Soc. 63, 1309–1313. https://doi.org/10.1175/1520-0477(1982)063<1309:scoteo>2.0.co;2.
Yan, H., Anthes, R.A., 1988. The effect of Variations in Surface Moisture on Mesoscale Circulation. Mon. Weather Rev. 116, 192–208. https://doi.org/10.1175/1520-0493(1988)116<0192:teovis>2.0.co;2.
Zavala-Hidalgo, J., Romero-Centeno, R., Mateos-Jasso, A., Morey, S.L., Martínez-López, B., 2014. The response of the Gulf of Mexico to wind and heat flux forcing: what has been learned in recent years? Atmosfera 27, 317–334. https://doi.org/10.1016/S0187-6236(14)71119-1.
Zhang, D., Anthes, R.A., 1982. A High-Resolution Model of the Planetary Boundary Layer—Sensitivity Tests and Comparisons with SESAME-79 Data. J. Appl. Meteorol. 21, 1594–1609. https://doi.org/10.1175/1520-0450(1982)021<1594:ahrmot>2.0.co;2.